Multiple sensor fault diagnosis for safe navigation of autonomous surface vessels

Dhyani, Abhishek; van der El, Kasper; Negenborn, Rudy R.; Reppa, Vasso

DOI
10.1016/j.conengprac.2025.106673

Publication date
2026

Document Version
Final published version

Published in
Control Engineering Practice

Control Engineering Practice 168 (2026) 106673

Contents lists available at ScienceDirect

Control Engineering Practice

journal homepage: www.elsevier.com/locate/conengprac

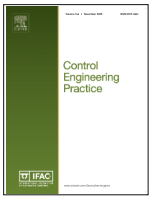

Multiple sensor fault diagnosis for safe navigation of autonomous surface vessels ⋆

Abhishek Dhyani [a,*], Kasper van der El [b], Rudy R. Negenborn [a], Vasso Reppa [a]

[a] Department of Maritime and Transport Technology, Delft University of Technology, The Netherlands
[b] Damen Research Development and Innovation BV, The Netherlands

ARTICLE INFO

Keywords:
Fault diagnosis
Nonlinear systems
Sensor systems
Marine navigation
Autonomous vehicles

ABSTRACT

Over the past decade, autonomous surface vessels (ASVs) have increasingly operated in a range of challenging environments involving safety-critical scenarios. Their navigational capabilities rely on rich and reliable sensor data, enabling accurate localisation, situational awareness and environmental perception. This allows ASVs to perform motion planning, collision avoidance and navigational control tasks. To ensure maritime safety, faults affecting onboard navigational sensors must be diagnosed.

This paper presents a model-based fault diagnosis scheme for ASVs affected by multiple sensor faults. Model-based methods utilise available sensors and dynamical models for residual generation. However, models describing the navigation may vary considerably for ASVs due to differences in vessel types, actuator configurations and sensor setups. To address this challenge, multiple residuals are synthesised using observer-based monitoring modules in the navigational sensors. Considering the impact of uncertainties, the residuals are designed to be bounded by adaptive thresholds proposed for each monitoring module. Fault isolation is then performed using a combinatorial decision logic, achieved by grouping the available sensors into multiple sensor sets and supported by model-based sensitivity analysis. Finally, the effectiveness of the proposed scheme is verified through simulation examples of two real-world vessels of different types with different sensor and actuator configurations, thereby illustrating its application.

1. Introduction

Integrating autonomy across different modes of transportation is expected to mitigate congestion and capacity constraints while enabling safer, more resilient and efficient transportation networks. For maritime operations, increasing the autonomy level could significantly enhance their economic viability by lowering operational costs and improving safety. A reduced onboard crew requirement for autonomous surface vessels (ASVs) not only facilitates deploying smaller and energy-efficient vessels but also reduces the risk of human injury in case of an accident. Nevertheless, for ASVs to serve as a viable solution, safety must be rigorously ensured.

Autonomous navigation is enabled by several heterogeneous sensors that provide essential data to localise and perceive their environment. Situational awareness underpins the decision-making processes that enable safe and efficient navigation in both open seas and inland waterways. Although autonomous navigation offers the potential to enhance safety compared to conventional (human-operated) navigation, any fault in the navigational sensors can result in serious consequences, such as damage to the vessel, infrastructure, or even human injury, making sensor fault diagnosis indispensable. Effective diagnostics enable timely remedial measures, such as activating redundant sensors or switching to a fault-tolerant control mode, ensuring that the operations continue with minimal disruption (Dhyani et al., 2024b).

Faults in sensor systems may arise from signal degradation due to environmental conditions or from a physical breakdown and can be either temporary or permanent. For example, a temporary fault might occur when the global navigation satellite system (GNSS) positional accuracy

⋆ The research leading to these results has received funding from the European Union's Horizon 2020 research and innovation programme under the Marie Skłodowska-Curie grant agreement No. 955768 (MSCA-ETN AUTOBarge), and Horizon Europe grant agreement No. 101202581 (WARRANT Project). This publication reflects only the authors' view, exempting the European Union and the granting authority from any liability. This research is also supported by the ResearchLab Autonomous Shipping (RAS) of TU Delft.

* Corresponding author.
E-mail addresses: a.dhyani-1@tudelft.nl (A. Dhyani), kasper.van.der.el@damen.com (K. van der El), r.r.negenborn@tudelft.nl (R.R. Negenborn), v.reppa@tudelft.nl (V. Reppa).

https://doi.org/10.1016/j.conengprac.2025.106673
Received 2 July 2025; Received in revised form 19 November 2025; Accepted 21 November 2025
Available online 27 November 2025

degrades due to obstacles such as buildings, bridges, or mountains that hinder satellite connectivity, but there is no physical breakdown. GNSS multipath effects can also introduce bias and significantly reduce measurement accuracy (Zidan et al., 2021). Various methods have been proposed in the literature to mitigate these issues; see, for example, Closas et al. (2009), Groves (2011). Additionally, signal spoofing and jamming, which are categorised as cyberattacks, pose serious safety risks. For example, a malicious agent might intercept and manipulate GNSS data, jeopardising the system's nominal operation. On the other hand, permanent faults may result from physical issues such as short circuits in sensor circuitry, Ethernet failure, or sensor wear and tear.

Current literature on fault diagnosis of marine navigation systems primarily employs model-based fault detection and isolation (FDI) schemes, which involve designing observers to generate residual signals indicative of potential faults. Many of these works propose approaches for diagnosing faults impacting the actuators; see, for example, Benetazzo et al. (2015), Bhagavathi et al. (2023), Cristofaro and Johansen (2014), Lin et al. (2018), Park and Yoo (2016), Song and He (2023), Tsolakis et al. (2024), Wang et al. (2020), Zhou et al. (2019). Wang et al. (2020) proposed an online fault estimator for ASVs affected by unknown faults and disturbances. The estimator can achieve finite-time tracking error convergence in the presence of actuator bias and partial loss of effectiveness faults. Park and Yoo (2016) proposed a robust fault detection observer and an adaptive fault accommodation scheme for saturated actuator faults affecting underactuated surface vessels. Cristofaro and Johansen (2014) presented an actuator and effector FDI and control reconfiguration scheme for overactuated systems by using unknown input observers. The proposed scheme is further verified by a case study on an overactuated vessel. In Tsolakis et al. (2024), an active isolation approach is proposed for an overactuated vessel with thruster faults, which can integrate with a traffic rule-compliant trajectory optimisation algorithm. Bhagavathi et al. (2023) proposed a digital twin-driven scheme for detecting and estimating faults in the vessel's propellers using an adaptive extended Kalman filter. Zhou et al. (2019) proposed an actuator fault diagnosis observer and a fault-tolerant controller for ASVs in a network environment with delays, packet dropouts and packet disordering. In Benetazzo et al. (2015), Lin et al. (2018), the problem of thruster fault diagnosis for the dynamic positioning (DP) of vessels is addressed following the parity space and observer-based approaches.

In addition to actuator fault diagnosis, addressing the sensor FDI problem is equally crucial, given the extensive number of sensors required for perception, situational awareness and state estimation. Furthermore, the harsh marine environment, characterised by conditions such as salt spray and high moisture levels, can accelerate sensor degradation (Liu et al., 2016). Some sensor FDI approaches, including those proposed by Blanke (2006), Rogne et al. (2014, 2015), and Asfihani et al. (2024), rely on simple kinematic models. Blanke (2006) proposed a structural analysis method that uses analytical redundancy relations (ARRs) to diagnose sensor faults and provide fault tolerance via sensor data fusion. Rogne et al. (2014, 2015) presented a sensor FDI scheme that relies on multiple nonlinear observers for vessels performing DP tasks. However, the aforementioned schemes do not account for the impact of external disturbances acting on the vessel. These factors can have a significant impact on diagnosis performance, leading to false alarms. Asfihani et al. (2024) proposed an adaptive Kalman filter-based method for sensor fault detection and estimation. The fault estimation, however, fails in some cases when the states linked to the sensor fault are not persistently excited.

On the other hand, sensor FDI schemes employing detailed dynamical models of the vessel have also been proposed (Wang et al., 2024; Zhang et al., 2021a,b). Zhang et al. (2021a) proposed an adaptive particle filter to ensure the robust navigation of unmanned vessels affected by faults in the navigational sensors and the propeller. A switching-mode hidden Markov model is used to describe the vessel model affected by possible fault modes. However, this approach lacks a theoretical verification of the estimation and diagnosis performance. In Zhang et al. (2021b), a nonlinear observer is proposed for sensor fault estimation in conjunction with a fault-tolerant model reference reinforcement learning control method that ensures stable tracking for ASVs affected by a sensor fault. A limitation of the proposed scheme is that it assumes the occurrence of a single fault. In Wang et al. (2024), an active fault-tolerant control scheme for ASVs is proposed for simultaneous sensor and actuator faults. The proposed method utilises a modified extended state observer and an adaptive output feedback control strategy, focusing on position-heading sensor faults. However, faults are modelled as a multiplicative factor with known bounds, limiting their scope of application.

External disturbances, such as winds, waves, and currents, can greatly impact vessel navigation, and their effects can lead to erroneous diagnostic results if not considered. In ports and inland waterways, wind forces are among the dominant external forces (Kepaptsoglou et al., 2015). Likewise, the vessel's motion and manoeuvrability are highly sensitive to water depth, which can vary in inland waterways and canals (Dhyani et al., 2025; Liu et al., 2015). Depth limitations impact the vessel's behaviour in various ways: they are perceptible in medium-deep water, highly significant in shallow water, and dominant in extremely shallow water (Vantorre et al., 2017). These factors, however, are neglected in existing model-based fault diagnosis schemes. Another key aspect that varies across vessels is the configuration of actuators and onboard sensors, which determines the dynamical model employed for residual generation in model-based FDI schemes.

In Dhyani et al. (2024a), the authors addressed these limitations by proposing a multiple-sensor FDI scheme for ASVs' navigational sensors. In the current article, the scheme is further extended, with the following key modifications:

1. Additional residuals are proposed for improved fault detectability, specifically, the residuals in the monitoring modules 3 and 4.
2. Through sensitivity analysis, the weak sensitivities of the faults to the residuals are identified. Consequently, an updated Fault Signature Matrix (FSM) is designed for improved fault isolability.

Overall, the main contributions of this work can be summarised as follows:

1. The design of the multiple-sensor FDI scheme for ASVs, as detailed in Section 3. While the FDI scheme in Dhyani et al. (2024a) focused on multiple residual generation based on the vessel's nonlinear dynamics, this work further extends the bank of residuals to enable fault diagnosis for a broad range of vessel characteristics. This is achieved by designing the residuals based on varying modelling complexity of the ASV, including a kinematic constraints model and a 3-degrees-of-freedom (DOF) hydrodynamic model (Section 2.1). Existing research on sensor FDI for ASVs based on detailed kinetic models is limited.
2. Adaptive thresholds are derived for bounding the generated residuals (Appendix B). Unlike fault detection schemes based on a constant threshold, adaptive thresholds are robust against noise and external disturbances affecting a vessel, ensuring that no false alarms occur. The influence of external disturbances, such as wind forces, shallow-water effects, and sensor noise, is also considered in the vessel modelling, as well as in the computation of the adaptive thresholds to improve sensor fault detectability (Appendix A). To the best of the authors' knowledge, these disturbances are not considered in the current FDI literature.
3. A fault signature matrix (FSM) is formulated by employing a combinatorial logic which is supported by model-based sensitivity analysis (Sections 3.3, 3.4). The resulting decision logic enables the isolation of multiple sensor faults.

The rest of the paper is structured as follows: In Section 2, the modelling of the vessel's maneuvering dynamics is presented. In Section 3, the design of the proposed sensor FDI scheme is detailed. In Section 4, the proposed scheme is verified through simulation studies involving

two vessel types: a pusher-barge inland vessel model with a propeller-rudder configuration and a catamaran-type ferry equipped with azimuth thrusters. Sensor FDI for these two vessels, which have different available models, sensors, and actuator configurations, is performed by utilising an appropriate selection of residuals. Finally, the conclusions and future research directions are reported in Section 5 of the paper. For the sake of notational convenience, the time variable t is omitted from all equations in this work, unless necessary, to avoid ambiguity. Further, all observer gains are assumed to be strictly positive/positive-definite to ensure convergence of the estimation errors.

2. Modelling for sensor fault diagnosis

Vessels are typically equipped with multiple redundant sensors for localisation and state estimation, complemented by processing methods to derive specific vessel states. Table 1 summarises the commonly used sensors for vessel navigation, with the respective data processing methods and the obtained parameters. A GNSS sensor determines the vessel's position $p = \begin{bmatrix} x_p & y_p \end{bmatrix}^T$, whereas the IMU, typically comprising an accelerometer, gyroscope/rate sensor, etc., provides the velocities ($v \in \mathbb{R}^3$). A gyrocompass measures the vessel's heading angle (ψ), and may be complemented by a magnetic compass. In some smaller vessels, a gyrocompass is replaced by a dual-antenna GNSS setup, as it allows for a sufficiently accurate heading angle estimation at a cheaper cost (Gade, 2016). The aforementioned parameters are obtained from the raw sensor outputs using sensor fusion and estimation methods, such as Kalman filtering, which form part of navigation devices like an inertial navigation system (INS) or the attitude heading reference system (AHRS). Further, a Doppler velocity log (DVL) and a speed log (or electromagnetic log) measure the vessel's speed through water (or ground) by utilising the Doppler effect and electromagnetic induction principles, respectively. The automatic identification system (AIS) integrates a GNSS antenna and provides the vessel's position, speed and course information, in addition to its other functions. GNSS-IMU sensor systems are ideal for vessel localisation due to their small size, low cost, and low energy consumption (Liu et al., 2016).

The sensor's outputs can be described by

$$\begin{aligned} S_{\text{pos}} &: y_{\text{pos}} = p + n_p + f_p \\ S_{\psi} &: y_{\psi} = \psi + n_{\psi} + f_{\psi} \\ S_{v} &: y_{v} = v + n_{v} + f_{v} \\ S_{\chi} &: y_{\chi} = \chi + n_{\chi} + f_{\chi}, \end{aligned} \tag{1}$$

where, $y_{\text{pos}} \in \mathbb{R}^2, y_{\psi} \in \mathbb{R}, y_v \in \mathbb{R}^3$ and $y_{\chi} \in \mathbb{R}$ correspond to the position p, heading angle ψ, velocities v, and the course angle χ, respectively. The vectors n and f represent the noise and fault(s) affecting these measurements.

In this work, permanent, persistent faults are considered. A sensor fault f_z occurring at a time instant T_{f_z} is modelled according to Reppa et al. (2016). Furthermore, the characteristics of a fault, defined by the fault function, the time of occurrence, and the evolution rate, are all treated as unknown in the design of the proposed scheme.

The objective of this work is to design a multiple-sensor FDI scheme for ASVs, accounting for the impact of external disturbances, sensor noise, and variations in sensor and actuator configurations.

2.1. Vessel maneuvering models

Vessel manoeuvring models can vary significantly in terms of complexity for a specific application. The availability of an accurate manoeuvring model with hydrodynamic characteristics is the foundation for model-based FDI. This section explores various models that can be used for generating residuals for FDI using the available sensor measurements and actuator/thrust information.

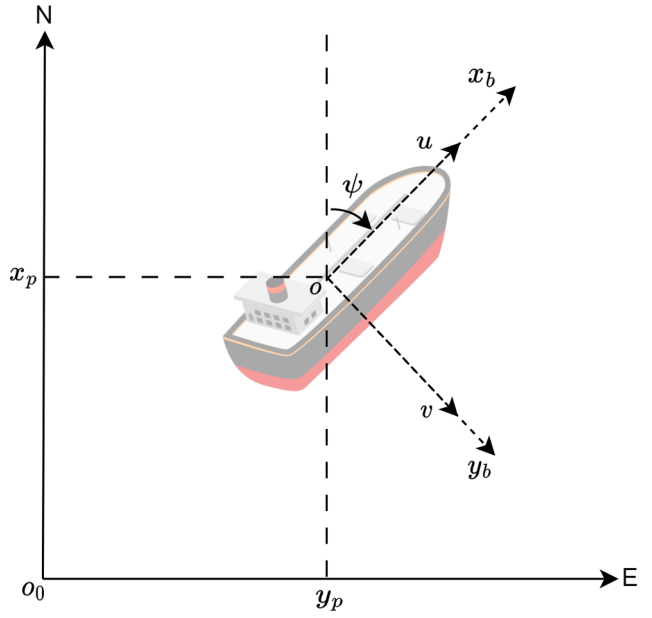

Fig. 1. The coordinate system of an ASV with the North-East-Down reference frame (o_0 – NED) and the body-fixed reference frame ($o - x_b y_b z_b$) (the D- and z_b-axes are not shown). (x_p, y_p) are the coordinates of the vessel's position in the o_0 frame. u, v and ψ are the surge and sway velocities and the heading angle, respectively.

2.1.1. Kinematic model

A vessel in motion satisfies kinematic constraints, which can provide information about the vessel's position and its heading, and have applications in target tracking (Tahk & Speyer, 1990) and path-following Fossen (2022). The kinematic constraints describe the relation of the vessel's velocities in the NED frame with its heading angle by

$$\begin{aligned} \dot{x}_p &= u\cos(\psi) - v\sin(\psi) \\ \dot{y}_p &= u\sin(\psi) + v\cos(\psi). \end{aligned} \tag{2}$$

In the amplitude-phase form, the above equations can be expressed as

$$\begin{aligned} \dot{x}_p &= U\cos(\psi + \beta_c) \\ \dot{y}_p &= U\sin(\psi + \beta_c), \end{aligned} \tag{3}$$

where $U = \sqrt{u^2 + v^2}$ is the speed in the horizontal plane and β_c is the crab angle. The course angle χ can be determined by filtering the position measurements, such as by employing a Kalman filter (Fossen, 2022), due to the relation

$$\chi = \tan^{-1}\left(\frac{\dot{y}_p}{\dot{x}_p}\right). \tag{4}$$

Similarly, the crab angle β_c can be calculated using the surge and sway velocities as

$$\beta_c = \tan^{-1}\left(\frac{v}{u}\right). \tag{5}$$

Finally, the heading angle can be expressed as

$$\psi = \chi - \beta_c. \tag{6}$$

Remark 1. It must be noted that the heading angle estimated using Equation (6) is accurate only for a moving vessel. This is because the horizontal crab angle formula (5) is numerically ill-conditioned for small values of surge and sway velocities. To address this issue, a numerically stable implementation is required, where crab angle calculations are discarded at low speeds.

2.1.2. 3-DOF maneuvering model

For many applications, the motion in a horizontal plane can be approximated by the following 3-DOF hydrodynamic model (see Fig. 1):

Table 1
Typically used sensors on vessels for localisation and state estimation, along with their corresponding measurements and the monitored parameters. These parameters are obtained post-processing using data processing methods as summarised below.

Sensor	Measured Parameter(s)	Data Processing Methods	Monitored Parameter(s) for Navigation
GNSS	Position (latitude, longitude, altitude)	Kalman Filtering, Low-pass Filtering, Sensor Fusion (e.g. with IMU)	Position in NED frame (x_p, y_p)
Dual-Antenna GNSS	Heading	Kalman Filtering, Sensor Fusion (e.g., with IMU)	Vessel heading (ψ)
IMU (accelerometer, gyroscope)	Linear accelerations and angular rates	Kalman Filtering, Sensor Fusion	Velocities in body frame (u, v, r)
Gyrocompass	Heading (true north reference)	Low-pass Filtering	Vessel heading (ψ)
Magnetic Compass	Heading (magnetic north reference)	Low-pass Filtering, Sensor Fusion (e.g. with gyrocompass)	Vessel heading (ψ)
Doppler Velocity Log (DVL)	Velocity through water or over ground in surge, sway directions	Kalman Filtering, Sensor Fusion (e.g. with GNSS)	Translational velocities in body frame (u, v)
Speed Log	Speed through water along the longitudinal axis (surge)	Low-pass Filtering, Sensor Fusion	Surge velocity in body frame (u)
AIS (Automatic Identification System)	Own vessel's speed over ground (SOG), course over ground (COG) and position (if integrated with onboard GNSS)	Low-pass Filtering, Sensor Fusion	Speed over ground (U), course over ground (χ) and position in NED frame (x_p, y_p)

$$\begin{bmatrix}\dot{\eta}\\ \dot{\nu}\end{bmatrix} = \begin{bmatrix}R(\psi)\nu\\ f(\nu,\tau)\end{bmatrix} + \begin{bmatrix}\mathbf{0}\\ \Delta(\eta,\nu)\end{bmatrix}, \tag{7}$$

where $\eta = \begin{bmatrix}x_p & y_p & \psi\end{bmatrix}^T$ is the generalised coordinate vector in the North-East-Down (NED) frame, and $\nu = \begin{bmatrix}u & v & r\end{bmatrix}^T$ is the generalised velocity vector in the body-fixed frame, with u, v denoting the linear velocities in surge and sway, and r denoting the angular velocity (yaw rate). The variable $\tau = \begin{bmatrix}\tau_u & \tau_v & \tau_r\end{bmatrix}^T$ represents the controlled input force vector. The term $R(\psi)$ represents the rotation matrix, described as

$$R(\psi) = \begin{bmatrix}\cos(\psi) & -\sin(\psi) & 0\\ \sin(\psi) & \cos(\psi) & 0\\ 0 & 0 & 1\end{bmatrix}. \tag{8}$$

Further, $f(\nu,\tau), \Delta(\eta,\nu) \in \mathbb{R}^3$ comprise the known and unknown nonlinear terms, respectively, described in two ways:

- In the Abkowitz model (Abkowitz, 1980; Fossen, 2011) it is

$$\begin{aligned} f(\nu,\tau) &= M^{-1}(-C(\nu)\nu - D(\nu)\nu + \tau)\\ \Delta(\eta,\nu) &= M^{-1}\tau_d, \end{aligned} \tag{9}$$

  where $\tau_d \in \mathbb{R}^3$ represents the added force vector, which models the impact of unknown forces acting on the vessel due to various external factors such as wind, currents and forces from the towing system (Du et al., 2021; Fossen & Strand, 1999). The term M represents the inertia matrix, which, under the assumption that the ship is port-starboard symmetric, can be described as

$$M = \begin{bmatrix}m + X_{\dot{u}} & 0 & 0\\ 0 & m - Y_{\dot{v}} & mx_G - Y_{\dot{r}}\\ 0 & mx_G - N_{\dot{v}} & I_{z_p} - N_{\dot{r}}\end{bmatrix}. \tag{10}$$

  Here m is the vessel's mass, I_{z_p} is the moment of inertia about the z_p-axis, and, $X_{\dot{u}}$, $Y_{\dot{v}}$, $Y_{\dot{r}}$, $N_{\dot{v}}$ and $N_{\dot{r}}$ are hydrodynamic parameters that account for the added mass. Further, x_G represents the x-coordinate of the vessel's centre of gravity. The terms $C(\nu)$, $D(\nu)$ are the Coriolis-centripetal and damping matrices given by equations (11) and (12), respectively.

$$C(\nu) = \begin{bmatrix}0 & 0 & -m(x_G r + v) + Y_{\dot{v}}v + Y_{\dot{r}}r\\ 0 & 0 & mu - X_{\dot{u}}u\\ m(x_G r + v) - Y_{\dot{v}}v - Y_{\dot{r}}r & -mu + X_{\dot{u}}u & 0\end{bmatrix} \tag{11}$$

$$D(\nu) = \begin{bmatrix}-X_u - X_{|u|u}|u| - X_{uuu}|u^2| & 0 & 0\\ 0 & -Y_v - Y_{|v|v}|v| - Y_{|r|v}|r| & -Y_r - Y_{|v|r}|v| - Y_{|r|r}|r|\\ 0 & -N_v - N_{|v|v}|v| - N_{|r|v}|r| & -N_r - N_{|v|r}|v| - N_{|r|r}|r|\end{bmatrix} \tag{12}$$

  Here, X_u, $X_{|u|u}$, X_{uuu}, Y_v, $Y_{|v|v}$, $Y_{|r|v}$, Y_r, $Y_{|v|r}$, $Y_{|r|r}$, N_v, $N_{|v|v}$, $N_{|r|v}$, N_r, $N_{|v|r}$ and $N_{|r|r}$, are the hydrodynamic parameters that account for the damping forces within the second-order modulus model representation (Fedyaevsky & Sobolev, 1964; Skjetne et al., 2004).
- In the Maneuvering Modeling Group (MMG) model, Ogawa et al. (1977), Yasukawa and Yoshimura (2015) it is

$$\begin{aligned} f(\nu,\tau) &= M'^{-1}(-D'(\nu) + \tau)\\ \Delta(\eta,\nu) &= M'^{-1}\tau_d. \end{aligned} \tag{13}$$

  Here, the matrices M' and $D'(\nu)$ are given as

$$\begin{aligned} M' &= \begin{bmatrix}(m + m_x) & 0 & 0\\ 0 & (m + m_y) & -x_G m_y\\ 0 & x_G m & (I_{z_p} + J_{z_p})\end{bmatrix}\\ D'(\nu) &= \begin{bmatrix}-(m + m_y)vr + x_G m_y r^2\\ (m + m_x)ur\\ x_G mur\end{bmatrix}, \end{aligned} \tag{14}$$

  where, m_x, m_y are the added masses in the x_p - and y_p - directions and J_{z_p} is the added moment of inertia for yaw motion. The assumption of port-starboard symmetry is applied again to obtain the matrix M' in this form.

Unlike the Abkowitz model in (9), where the hydrodynamic forces and moments are aggregated into the damping and Coriolis matrices (11),(12), in the MMG model, the hydrodynamic forces are decomposed into individual terms arising from the hull, propeller, and rudder. This approach is often more suitable for assessing the impact of these different components on the vessel's maneuverability. However, it is based on the assumption that the vessel has a conventional propeller and rudder configuration.

The vessel's actuation system is directly responsible for controlling its maneuvering motion. Therefore, its dynamics and configuration must be accurately modelled to simulate realistic vessel behaviour. For a twin azimuth-thruster configuration, the controlled input force vector can be

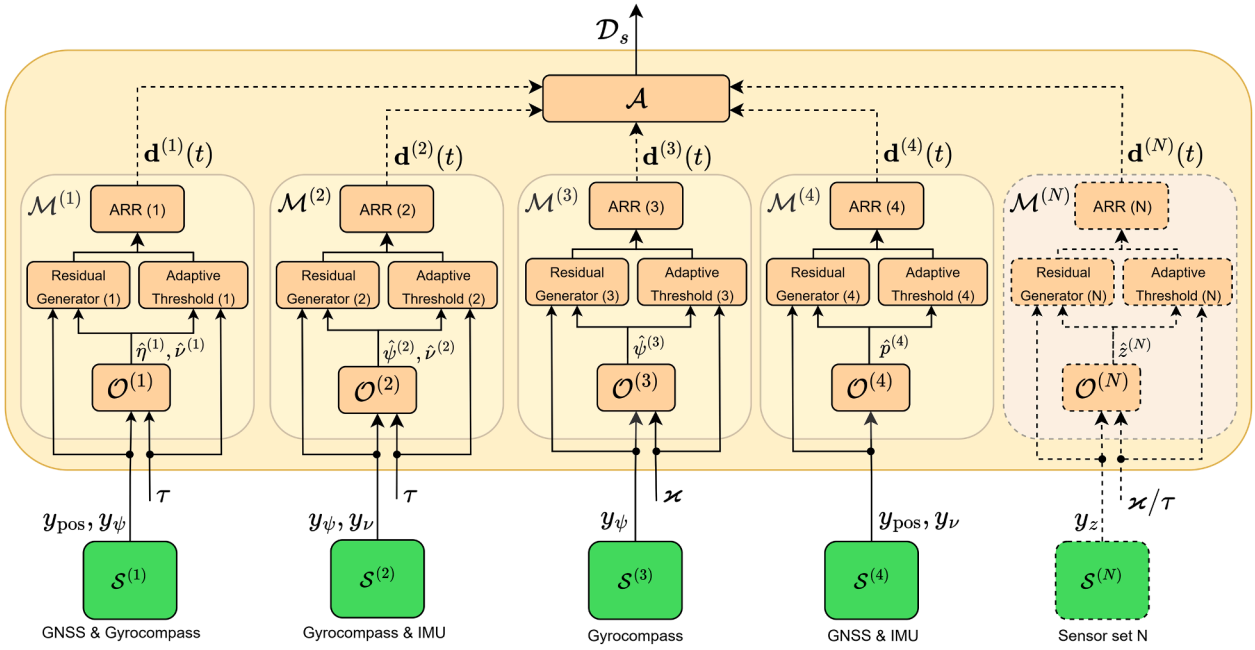

Fig. 2. Proposed architecture of the sensor fault detection and isolation scheme.

defined as Marley et al. (2023)

$$\tau = \begin{bmatrix} \tau_u \\ \tau_v \\ \tau_r \end{bmatrix} = \begin{bmatrix} X_{\text{pr},1} + X_{\text{pr},2} \\ Y_{\text{pr},1} + Y_{\text{pr},2} \\ N_{\text{pr},1} + N_{\text{pr},2} \end{bmatrix}, \tag{15}$$

where, $X_{\text{pr},w}$, $Y_{\text{pr},w}$ and $N_{\text{pr},w}$ are the generalised force components for each thruster, with $w \in \{1, 2\}$. For the rudder-propeller configuration, the controlled input force vector is given by

$$\tau = \begin{bmatrix} \tau_1 \\ \tau_2 \\ \tau_3 \end{bmatrix} = \begin{bmatrix} X_P + X_R \\ Y_R \\ N_R \end{bmatrix}, \tag{16}$$

where, X_R represents the forward force, Y_R the lateral force, and N_R the yaw moment component due to the rudder. Further, X_P represents the forward force component from the ship's propeller.

2.1.3. Steering model

The steering or KT model, attributed to Nomoto et al. (1957), is a popular linear modelling approach that can sufficiently capture the turning and course-keeping behaviour of the vessel. It is a 1-DOF model that assumes constant surge and sway velocities; therefore, it is not a complete replacement of the aforementioned 3-DOF hydrodynamic models. This work focuses on its second-order form, a common variant that supports overshooting behaviour and offers higher accuracy compared to the first-order form. For an azimuth-type twin-thruster configuration, it can be described by

$$\begin{aligned} &\ddot{r} + a_1\dot{r} + a_2 r = b_1(b_2\dot{\delta_p} + \delta_p) + b_3(b_4\dot{\delta_s} + \delta_s) \\ &\dot{\psi} = r,\ \dot{u} = 0,\ \dot{v} = 0, \end{aligned} \tag{17}$$

where δ_p and δ_s are the thruster angles for the port and starboard sides, and $a_{(.)}$, $b_{(.)}$ represent the parameters related to yaw rate and thruster angles, respectively. These parameters can be determined using the vessel's operational data from free-running tests involving zigzag and/or turning circle maneuvers.

3. Sensor fault detection and isolation scheme

In this section, the design of the proposed multiple-sensor FDI scheme is discussed in detail. Firstly, to enable the isolation of multiple sensor faults, the considered sensors are decomposed into N sensor sets $S^{(I)}, I = 1, \ldots, N$ (Reppa et al., 2016). A monitoring module $\mathcal{M}^{(I)}$ is employed, composed of an observer to estimate the measurements corresponding to each sensor set. Further, every monitoring module contains a set of analytical redundancy relations (ARRs) that detect the occurrence of faults. Designing monitoring modules for the isolation of multiple faulty sensors is particularly challenging, as it requires that each monitoring module be selectively sensitive to a subset of possible sensor faults. This can introduce challenges in the observer design due to a potential loss of observability. To overcome this issue and enhance isolability, the sensor sets are designed to be overlapping, i.e., some sensors belong to more than one sensor set.

As shown in Fig. 2, the monitoring module $\mathcal{M}^{(I)}$ comprises observers denoted by $\mathcal{O}^{(I)}$, which are used to generate the residuals. A residual is a signal that describes the difference between observed system behaviour (using sensors) and the expected one (using observers). Within each module, the ARRs are computed and subsequently, the decisions $\mathbf{d}^{(I)}$, which are binary vectors representing the fault detection results. Adaptive thresholds are derived to compute the ARRs while accounting for sensor noise, as well as external factors described in Appendix A. Finally, the decisions obtained based on the satisfaction or violation of the ARRs are provided to the aggregator module $\mathcal{A}$, which computes the set of possibly occurring (multiple) fault(s) $\mathcal{D}_s$, thereby isolating the faulty sensor(s).

In this work, the decomposition of sensors is performed such that $N = 4$. The resulting sensor sets are defined by

$$\begin{aligned} S^{(1)} &= \{S^{(1,1)}, S^{(1,2)}\} = \{S_{\text{pos}}, S_\psi\} \\ S^{(2)} &= \{S^{(2,1)}, S^{(2,2)}\} = \{S_\psi, S_v\} \\ S^{(3)} &= \{S^{(3,1)}\} = \{S_\psi\} \\ S^{(4)} &= \{S^{(4,1)}\} = \{S_{\text{pos}}, S_v\}. \end{aligned} \tag{18}$$

This decomposition facilitates designing observers that are selectively sensitive to sensor faults, as shown in the subsequent sections. The corresponding monitoring modules are given by $\mathcal{M}^{(1)} - \mathcal{M}^{(4)}$, respectively, and are responsible for (a) GNSS and gyrocompass, (b) gyrocompass and IMU, (c) gyrocompass only, and (d) GNSS sensors only. While the monitoring modules $\mathcal{M}^{(1)} - \mathcal{M}^{(3)}$ employ observers based on both the sensor measurements and controlled inputs (generalised forces/thruster angles) for residual generation, the observer in module $\mathcal{M}^{(4)}$ utilises only

the sensor measurements. Depending on the sensor setup, a sensor set and the corresponding monitoring module may be discarded, or additional monitoring modules may be integrated for residual generation. For example, using an available, more "reliable" redundant sensor can help improve fault isolability (Rogne et al., 2014; Zhang et al., 2024b).

3.1. Observer design

This subsection details the design of a bank of Luenberger-type observers for performing sensor FDI. The design enables structured sensitivity against the set of possible faults. Firstly, the monitoring module $\mathcal{M}^{(1)}$ is considered for monitoring the GNSS and gyrocompass sensors, having the observer dynamics given by

$$\mathcal{O}^{(1)}: \begin{aligned} \dot{\hat{\eta}}^{(1)} &= R(\hat{\psi}^{(1)})\hat{\nu}^{(1)} + K_1\tilde{\eta}^{(1)} \\ \dot{\hat{\nu}}^{(1)} &= f(\hat{\nu}^{(1)}, \tau) + K_2 R^T(\hat{\psi}^{(1)})\tilde{\eta}^{(1)}, \end{aligned} \tag{19}$$

where, $\hat{\eta}^{(1)}$, $\hat{\nu}^{(1)}$ and $\hat{\psi}^{(1)}$ denote the estimations of $\eta = \begin{bmatrix} p & \psi \end{bmatrix}^T$, ν and ψ, respectively, and $\tilde{\eta}^{(1)} = y_\eta - \hat{\eta}^{(1)}$, where $y_\eta = \begin{bmatrix} y_{\text{pos}} & y_\psi \end{bmatrix}^T$. The term $f(\hat{\nu}^{(1)}, \tau)$ is given by Equation (9) or (13), according to the selected modelling approach. The observer gains K_1 and $K_2 \in \mathbb{R}^{3\times3}$ are positive diagonal matrices.

The monitoring module $\mathcal{M}^{(2)}$, designed for the gyrocompass and IMU, comprises the observer $\mathcal{O}^{(2)}$, given by

$$\mathcal{O}^{(2)}: \begin{aligned} \dot{\hat{\psi}}^{(2)} &= \hat{r}^{(2)} + k_3\tilde{\psi}^{(2)} \\ \dot{\hat{\nu}}^{(2)} &= f(\hat{\nu}^{(2)}, \tau) + K_4\tilde{\nu}^{(2)}, \end{aligned} \tag{20}$$

where, $\tilde{\psi}^{(2)} = y_\psi - \hat{\psi}^{(2)}$ and $\tilde{\nu}^{(2)} = y_\nu - \hat{\nu}^{(2)}$ are the output estimation errors for ψ and ν, respectively. Here, $k_3 \in \mathbb{R}$, and $K_4 \in \mathbb{R}^{3\times3}$ is a diagonal gain matrix.

Remark 2. Note that the observers $\mathcal{O}^{(1)}$ and $\mathcal{O}^{(2)}$ are independent of the sensor measurements y_ν and y_{pos}, respectively. As a result, the residuals computed in the monitoring modules $\mathcal{M}^{(1)}$ and $\mathcal{M}^{(2)}$ are structurally sensitive only to a desired subset of faults.

The monitoring module $\mathcal{M}^{(3)}$ is based on a linear observer $\mathcal{O}^{(3)}$, which is derived from the second-order steering model given by (17). The observer dynamics are given as

$$\mathcal{O}^{(3)}: \begin{aligned} \begin{bmatrix} \dot{\hat{\psi}}^{(3)} \\ \ddot{\hat{\psi}}^{(3)} \\ \dddot{\hat{\psi}}^{(3)} \end{bmatrix} &= \begin{bmatrix} 0 & 1 & 0 \\ 0 & 0 & 1 \\ 0 & -a_2 & -a_1 \end{bmatrix} \begin{bmatrix} \hat{\psi}^{(3)} \\ \dot{\hat{r}}^{(3)} \\ \ddot{\hat{r}}^{(3)} \end{bmatrix} + \\ & \begin{bmatrix} 0 & 0 & 0 & 0 \\ 0 & 0 & 0 & 0 \\ b_1 & b_1b_2 & b_3 & b_3b_4 \end{bmatrix} \begin{bmatrix} \delta_p \\ \dot{\delta}_p \\ \delta_s \\ \dot{\delta}_s \end{bmatrix} + \begin{bmatrix} k_5 \\ 0 \\ 0 \end{bmatrix} \tilde{\psi}^{(3)} \end{aligned} \tag{21}$$

where $\tilde{\psi}^{(3)} = y_\psi - \hat{\psi}^{(3)}$ is the output estimation error for ψ, $a_{(.)}$ and $b_{(.)}$ are the identified parameters of the steering model, and $k_5 \in \mathbb{R}$ is the observer gain. Note that unlike the observers $\mathcal{O}^{(1)}$ and $\mathcal{O}^{(2)}$, $\mathcal{O}^{(3)}$ takes the thruster angles and their derivatives as inputs, represented by $\varkappa = \begin{bmatrix} \delta_p & \dot{\delta}_p & \delta_s & \dot{\delta}_s \end{bmatrix}^T$.

Remark 3. For the rudder-propeller configuration, the observer $\mathcal{O}^{(3)}$ can be given by

$$\mathcal{O}^{(3)}: \begin{aligned} \begin{bmatrix} \dot{\hat{\psi}}^{(3)} \\ \ddot{\hat{\psi}}^{(3)} \\ \dddot{\hat{\psi}}^{(3)} \end{bmatrix} &= \begin{bmatrix} 0 & 1 & 0 \\ 0 & 0 & 1 \\ 0 & -\frac{1}{T_1T_2} & -\frac{T_1+T_2}{T_1T_2} \end{bmatrix} \begin{bmatrix} \hat{\psi}^{(3)} \\ \dot{\hat{r}}^{(3)} \\ \ddot{\hat{r}}^{(3)} \end{bmatrix} + \\ & \frac{K}{T_1T_2} \begin{bmatrix} 0 & 0 \\ 0 & 0 \\ 1 & T_3 \end{bmatrix} \begin{bmatrix} \delta \\ \dot{\delta} \end{bmatrix} + \begin{bmatrix} k_5 \\ 0 \\ 0 \end{bmatrix} \tilde{\psi}^{(3)}, \end{aligned} \tag{22}$$

and the input of the monitoring module $\mathcal{M}^{(3)}$ becomes $\varkappa = \begin{bmatrix} \delta & \dot{\delta} \end{bmatrix}^T$. Here, the terms T_1, T_2, and T_3 denote the time constants, and K denotes the gain factor.

Finally, the monitoring module $\mathcal{M}^{(4)}$ is designed using only GNSS (or AIS) and IMU measurements. Firstly, the vessel's heading angle is calculated as a function of its course and crab angles, and it is given by

$$y_\psi = y_\chi - \tan^{-1}\left(\frac{y_v}{y_u}\right), \tag{23}$$

where y_u, y_v are the surge and sway velocity measurements and y_χ is the course angle measurement provided by the GNSS or the AIS. Using the heading angle measurement (y_ψ), and the velocity measurements (y_u, y_v), the observer dynamics $\mathcal{O}^{(4)}$ can be described by

$$\mathcal{O}^{(4)}: \begin{aligned} \dot{\hat{x}}_p^{(4)} &= y_u\cos(y_\psi) - y_v\sin(y_\psi) + k_{61}\tilde{x}_p^{(4)} \\ \dot{\hat{y}}_p^{(4)} &= y_u\sin(y_\psi) + y_v\cos(y_\psi) + k_{62}\tilde{y}_p^{(4)}, \end{aligned} \tag{24}$$

where, $\tilde{x}_p^{(4)} = y_{x_p} - \hat{x}_p^{(4)}$, $\tilde{y}_p^{(4)} = y_{y_p} - \hat{y}_p^{(4)}$, with y_{x_p} and y_{y_p} denoting the position measurements, and $k_{61}, k_{62} \in \mathbb{R}$.

3.2. Residual generator design

Using the observers defined in the previous subsection, the residuals are generated, and their corresponding adaptive thresholds are computed within the respective monitoring modules. Let us define $z^{(I)}, I = 1, \dots, 4$, to be vectors consisting of the vessel states such that $z^{(1)} = \begin{bmatrix} p & \psi & \nu \end{bmatrix}^T$, $z^{(2)} = \begin{bmatrix} \psi & \nu \end{bmatrix}^T$, $z^{(3)} = \psi$ and $z^{(4)} = \begin{bmatrix} p & \nu \end{bmatrix}^T$. The residual vector $\varepsilon_{y_z}^{(I)} \in \mathbb{R}^{N_I}$ is defined by

$$\varepsilon_{y_z}^{(I)} = y_z^{(I)} - \hat{z}^{(I)}, \tag{25}$$

where, $y_z^{(I)}$ and $\hat{z}^{(I)}$ represent the measurements and estimations of the vectors $z^{(I)}$ in the $I-$th monitoring module, respectively. The superscript $\{.\}^{(j)}$ will be used to signify that the residual corresponds to the $j-$th sensor, $j \in \{1, \dots, m_I\}$, where m_I denotes the no. of sensors in the $I-$th sensor set. In this work, $m_I = 2$, for the sensor sets $\mathcal{S}^{(1)}, \mathcal{S}^{(2)}$, and $m_I = 1$, for the sensor sets $\mathcal{S}^{(3)}$ and $\mathcal{S}^{(4)}$, respectively. The corresponding residual vectors are given by

$$\begin{aligned} \varepsilon_{y_z}^{(1)} &= \begin{bmatrix} \varepsilon_{y_z}^{(1,1)} \\ \varepsilon_{y_z}^{(1,2)} \end{bmatrix} = \begin{bmatrix} y_{\text{pos}} \\ y_\psi \end{bmatrix} - \begin{bmatrix} \hat{z}^{(1,1)} \\ \hat{z}^{(1,2)} \end{bmatrix} \\ \varepsilon_{y_z}^{(2)} &= \begin{bmatrix} \varepsilon_{y_z}^{(2,1)} \\ \varepsilon_{y_z}^{(2,2)} \end{bmatrix} = \begin{bmatrix} y_\psi \\ y_\nu \end{bmatrix} - \begin{bmatrix} \hat{z}^{(2,1)} \\ \hat{z}^{(2,2)} \end{bmatrix} \\ \varepsilon_{y_z}^{(3)} &= \varepsilon_{y_z}^{(3,1)} = y_\psi - \hat{z}^{(3,1)} \\ \varepsilon_{y_z}^{(4)} &= \varepsilon_{y_z}^{(4,1)} = y_{\text{pos}} - \hat{z}^{(4,1)}, \end{aligned} \tag{26}$$

where $\begin{bmatrix} \hat{z}^{(1,1)} & \hat{z}^{(1,2)} \end{bmatrix}^T = \begin{bmatrix} \hat{p} & \hat{\psi} \end{bmatrix}^T$, $\begin{bmatrix} \hat{z}^{(2,1)} & \hat{z}^{(2,2)} \end{bmatrix}^T = \begin{bmatrix} \hat{\psi} & \hat{\nu} \end{bmatrix}^T$, $\hat{z}^{(3,1)} = \hat{\psi}$ and $\hat{z}^{(4,1)} = \hat{p}$ are generated by the observers $\mathcal{O}^{(1)}$,..., $\mathcal{O}^{(4)}$, respectively. Under healthy conditions (absence of faults), the residual components $\varepsilon_{y_zH}^{(I,j)}$ are described by

$$\varepsilon_{y_zH}^{(I,j)} = y_{z_jH} - \hat{z}_H^{(I,j)}, \tag{27}$$

with y_{z_jH} denoting the healthy sensor measurement of the state $z^{(I,j)}$. The $j-$th adaptive threshold is defined by $\bar{\varepsilon}_{y_z}^{(I,j)}$, for $I \in \{1, \dots, 4\}$ and $j \in \{1, \dots, m_I\}$, respectively. Under healthy conditions, it is denoted by $\bar{\varepsilon}_{y_zH}^{(I,j)}$ and must be computed such that

$$|\varepsilon_{y_zH}^{(I,j)}| \leq \bar{\varepsilon}_{y_zH}^{(I,j)}. \tag{28}$$

The following design criteria are adopted to compute the adaptive thresholds $\bar{\varepsilon}_{y_z}^{(I,j)}$ and subsequently, the ARRs:

1. The thresholds must be robust to uncertainties, thereby ensuring that no false alarms occur, i.e., if $\mathcal{S}^{(I)}$ is not affected by faults, then the corresponding set of ARRs must always be satisfied.
2. The ARRs must be structurally sensitive to the occurrence of one or more sensor faults, i.e., if at any time instant t, the set of ARRs is not satisfied, then the occurrence of at least one sensor fault in $\mathcal{S}^{(I)}$ must be guaranteed.

To compute adaptive thresholds that satisfy these criteria, firstly, $\varepsilon_{y_z H}^{(I,j)}$ can be expressed in terms of the state estimation error under healthy conditions $\varepsilon_{zH}^{(I,j)}$ as

$$\varepsilon_{y_z H}^{(I,j)} = \varepsilon_{zH}^{(I,j)} + n_z^{(I,j)}, \tag{29}$$

with, $\varepsilon_{zH}^{(I,j)} = z^{(I,j)} - \hat{z}_H^{(I,j)}$. Under healthy conditions, the following assumptions regarding the vessel dynamics and sensor noise are considered:

Assumption 1. The input force τ remains bounded before and after the occurrence of multiple sensor faults, i.e., there exist some compact stability region $\mathcal{R}^{\tau} \subset \mathbb{R}^3$ such that $\tau \in \mathcal{R}^{\tau}$, for all $t \geq 0$.

Assumption 2. The unknown noise affecting the $j-$th sensor ($n_z^{(I,j)}$) is uniformly bounded, i.e., $|n_{z_k}^{(I,j)}| \leq \bar{n}_{z_k}^{(I,j)}$, for all k elements of $n_z^{(I,j)}$, with $\bar{n}_{z_k}^{(I,j)}$ representing a known bound.

These assumptions represent realistic system behaviour under healthy conditions while ensuring the convergence of the residual signals. As a result, the magnitudes of the residual components are bounded by

$$\begin{aligned}
\begin{bmatrix} |\varepsilon_{y_z H}^{(1,1)}| \\ |\varepsilon_{y_z H}^{(1,2)}| \end{bmatrix} &\leq \begin{bmatrix} |\varepsilon_{zH}^{(1,1)}| \\ |\varepsilon_{zH}^{(1,2)}| \end{bmatrix} + \begin{bmatrix} \bar{n}_z^{(1,1)} \\ \bar{n}_z^{(1,2)} \end{bmatrix} \\
\begin{bmatrix} |\varepsilon_{y_z H}^{(2,1)}| \\ |\varepsilon_{y_z H}^{(2,2)}| \end{bmatrix} &\leq \begin{bmatrix} |\varepsilon_{zH}^{(2,1)}| \\ |\varepsilon_{zH}^{(2,2)}| \end{bmatrix} + \begin{bmatrix} \bar{n}_z^{(2,1)} \\ \bar{n}_z^{(2,2)} \end{bmatrix} \\
|\varepsilon_{y_z H}^{(3,1)}| &\leq |\varepsilon_{zH}^{(3,1)}| + \bar{n}_z^{(3,1)} \\
|\varepsilon_{y_z H}^{(4,1)}| &\leq |\varepsilon_{zH}^{(4,1)}| + \bar{n}_z^{(4,1)},
\end{aligned} \tag{30}$$

where $|\varepsilon_{zH}^{(I,j)}|$ are the estimation error magnitudes for the states in the vectors $z^{(I)}$, respectively.

Further, the dynamics governing the state estimation error of the observer $\mathcal{O}^{(1)}$ can be described by

$$\begin{aligned}
\dot{\varepsilon}_{zH}^{(1)} &= \begin{bmatrix} \dot{\varepsilon}_{zH}^{(1,1)} \\ \dot{\varepsilon}_{zH}^{(1,2)} \\ \dot{\varepsilon}_{zH}^{(1,3)} \end{bmatrix} = \begin{bmatrix} -K_{11} & \mathbf{0} & \mathbf{0} \\ \mathbf{0} & -k_{12} & \mathbf{0} \\ \mathbf{0} & \mathbf{0} & -K_2 \end{bmatrix} \begin{bmatrix} \varepsilon_{zH}^{(1,1)} \\ \varepsilon_{zH}^{(1,2)} \\ \varepsilon_{zH}^{(1,3)} \end{bmatrix} + \begin{bmatrix} \tilde{\gamma}_{1H}^{(1)} \\ \tilde{\gamma}_{2H}^{(1)} \end{bmatrix} \\
&\quad + \begin{bmatrix} \mathbf{0} \\ \Delta(\eta,\nu) + K_2 \nu \end{bmatrix} + \begin{bmatrix} -K_{11} & \mathbf{0} & \mathbf{0} \\ \mathbf{0} & -k_{12} & \mathbf{0} \\ \mathbf{0} & \mathbf{0} & -K_2 \end{bmatrix} \begin{bmatrix} n_z^{(1,1)} \\ n_z^{(1,2)} \\ R^T(\hat{\psi}_H^{(1)}) y_\eta \end{bmatrix},
\end{aligned} \tag{31}$$

where $\tilde{\gamma}_{1H}^{(1)} = R(\psi)\nu - R(\hat{\psi}_H^{(1)})\hat{\nu}_H^{(1)}$, $\tilde{\gamma}_{2H}^{(1)} = f(\nu,\tau) - f(\hat{\nu}_H^{(1)},\tau)$, and $\mathbf{0}$ denotes a matrix/vector of zeroes, having a suitable dimension. Solving (31) results in

$$\begin{aligned}
\varepsilon_{zH}^{(1)} &= \begin{bmatrix} \varepsilon_{zH}^{(1,1)} \\ \varepsilon_{zH}^{(1,2)} \\ \varepsilon_{zH}^{(1,3)} \end{bmatrix} = \begin{bmatrix} e^{-K_{11}t} & \mathbf{0} & \mathbf{0} \\ \mathbf{0} & e^{-k_{12}t} & \mathbf{0} \\ \mathbf{0} & \mathbf{0} & e^{-K_2 t} \end{bmatrix} \begin{bmatrix} \varepsilon_{zH}^{(1,1)}(0) \\ \varepsilon_{zH}^{(1,2)}(0) \\ \varepsilon_{zH}^{(1,3)}(0) \end{bmatrix} \\
&\quad + \int_0^t \begin{bmatrix} e^{-K_1(t-\mathrm{t})} & \mathbf{0} \\ \mathbf{0} & e^{-K_2(t-\mathrm{t})} \end{bmatrix} \left(\begin{bmatrix} \tilde{\gamma}_{1H}^{(1)}(\mathrm{t}) \\ \tilde{\gamma}_{2H}^{(1)}(\mathrm{t}) + \Delta(\eta,\nu) \end{bmatrix} \right. \\
&\quad \left. + \begin{bmatrix} -K_1 n_\eta \\ -K_2 R^T(\hat{\psi}_H^{(1)}(\mathrm{t})) n_\eta + K_2(\nu(\mathrm{t}) - R^T(\hat{\psi}_H^{(1)}(\mathrm{t}))\eta(\mathrm{t})) \end{bmatrix} \right) d\mathrm{t},
\end{aligned} \tag{32}$$

where $K_1 = \mathrm{diag}(\begin{bmatrix} K_{11} & k_{12} \end{bmatrix})$, $n_\eta = \begin{bmatrix} n_z^{(1,1)} & n_z^{(1,2)} \end{bmatrix}^T$. Using the above equation and the relation in (29), the residuals in $\varepsilon_{y_z}^{(1)}$ under healthy conditions can be expressed by

$$\begin{aligned}
\begin{bmatrix} \varepsilon_{y_z H}^{(1,1)} \\ \varepsilon_{y_z H}^{(1,2)} \end{bmatrix} &= e^{-K_1 t} \begin{bmatrix} \varepsilon_{zH}^{(1,1)}(0) \\ \varepsilon_{zH}^{(1,2)}(0) \end{bmatrix} + \begin{bmatrix} n_z^{(1,1)} \\ n_z^{(1,2)} \end{bmatrix} \\
&\quad + \int_0^t e^{-K_1(t-\mathrm{t})} \left(\tilde{\gamma}_{1H}^{(1)}(\mathrm{t}) - K_1 n_\eta \right) d\mathrm{t}.
\end{aligned} \tag{33}$$

In addition to the Assumptions 1 and 2, the following assumption regarding the uncertainties is considered:

Assumption 3. The unknown added force vector τ_d is uniformly bounded, i.e., $|\tau_{d_i}| \leq \bar{\tau}_{d_i}$, with $i \in \{1,2,3\}$ representing the elements of the vector and $\bar{\tau}_{d_i}$ representing a known bound.

Assumption 3 provides a bound to distinguish the uncertainties from the faults and holds practically for a vessel operating within specified operational conditions (wind limits, sea state, speed range, etc.). Under this assumption, bounds on the magnitudes of the state estimation errors are derived, as detailed in the Appendix B.

For the observer $\mathcal{O}^{(2)}$, the state estimation error dynamics are given by

$$\begin{aligned}
\dot{\varepsilon}_{zH}^{(2)} &= \begin{bmatrix} \dot{\varepsilon}_{zH}^{(2,1)} \\ \dot{\varepsilon}_{zH}^{(2,2)} \end{bmatrix} = \begin{bmatrix} -k_3 & \mathbf{0} \\ \mathbf{0} & -K_4 \end{bmatrix} \begin{bmatrix} \varepsilon_{zH}^{(2,1)} \\ \varepsilon_{zH}^{(2,2)} \end{bmatrix} + \begin{bmatrix} \tilde{\gamma}_{1H}^{(2)} \\ \tilde{\gamma}_{2H}^{(2)} + \Delta(\eta,\nu) \end{bmatrix} \\
&\quad + \begin{bmatrix} -k_3 & \mathbf{0} \\ \mathbf{0} & -K_4 \end{bmatrix} \begin{bmatrix} n_z^{(2,1)} \\ n_z^{(2,2)} \end{bmatrix},
\end{aligned} \tag{34}$$

where $\tilde{\gamma}_{1H}^{(2)} = r - \hat{r}_H$, and $\tilde{\gamma}_{2H}^{(2)} = f(\nu,\tau) - f(\hat{\nu}_H^{(2)},\tau)$. The resulting residuals in $\varepsilon_{y_z}^{(2)}$ under healthy conditions can be expressed by

$$\begin{aligned}
\begin{bmatrix} \varepsilon_{y_z H}^{(2,1)} \\ \varepsilon_{y_z H}^{(2,2)} \end{bmatrix} &= \begin{bmatrix} e^{-k_3 t} & \mathbf{0} \\ \mathbf{0} & e^{-K_4 t} \end{bmatrix} \begin{bmatrix} \varepsilon_{zH}^{(2,1)}(0) \\ \varepsilon_{zH}^{(2,2)}(0) \end{bmatrix} \\
&\quad + \begin{bmatrix} n_z^{(2,1)} \\ n_z^{(2,2)} \end{bmatrix} + \int_0^t \begin{bmatrix} e^{-k_3(t-\mathrm{t})} & \mathbf{0} \\ \mathbf{0} & e^{-K_4(t-\mathrm{t})} \end{bmatrix} \\
&\quad \left(\begin{bmatrix} \tilde{\gamma}_{1H}^{(2)}(\mathrm{t}) - k_3 n_z^{(2,1)} \\ \tilde{\gamma}_{2H}^{(2)}(\mathrm{t}) + \Delta(\eta,\nu) - K_4 n_z^{(2,2)} \end{bmatrix} \right) d\mathrm{t}.
\end{aligned} \tag{35}$$

Next, the adaptive threshold corresponding to the residual in $\mathcal{M}^{(3)}$ is derived. The state estimation error for the observer $\mathcal{O}^{(3)}$ can be described under healthy conditions by

$$\begin{aligned}
\dot{\varepsilon}_{zH}^{(3,1)} &= -k_5 \varepsilon_{zH}^{(3,1)} + \dot{\psi}_H + \frac{1}{a_2}\dddot{\psi}^{(3)} + \frac{a_1}{a_2}\ddot{\psi}^{(3)} \\
&\quad - \frac{b_1}{a_2}(b_2 \dot{\delta}_p + \delta_p) - \frac{b_3}{a_2}(b_4 \dot{\delta}_s + \delta_s) - k_5 n_z^{(3,1)}.
\end{aligned} \tag{36}$$

The resulting residual under healthy conditions ($\varepsilon_{y_z H}^{(3,1)}$) is expressed by

$$\begin{aligned}
\varepsilon_{y_z H}^{(3,1)} &= e^{-k_5 t} \varepsilon_{zH}^{(3,1)}(0) + n_z^{(3,1)} + \int_0^t e^{-k_5(t-\mathrm{t})} \left(\dot{\psi}_H \right. \\
&\quad \left. + \frac{1}{a_2}\dddot{\psi}^{(3)} + \frac{a_1}{a_2}\ddot{\psi}^{(3)} - \frac{b_1}{a_2}(b_2 \dot{\delta}_p + \delta_p) - \frac{b_3}{a_2}(b_4 \dot{\delta}_s + \delta_s) - k_5 n_z^{(3,1)} \right) d\mathrm{t}.
\end{aligned} \tag{37}$$

Finally, for the observer $\mathcal{O}^{(4)}$, the state estimation error dynamics under healthy conditions can be described by

$$\begin{aligned}
\dot{\varepsilon}_{zH}^{(4,1)} &= -K_6 \varepsilon_{zH}^{(4,1)} \\
&\quad + \begin{bmatrix} u(\cos\psi - \cos y_\psi^{(4)}) + v(-\sin\psi + \sin y_\psi^{(4)}) \\ u(\sin\psi - \sin y_\psi^{(4)}) + v(\cos\psi - \cos y_\psi^{(4)}) \end{bmatrix} \\
&\quad + \begin{bmatrix} -\cos y_\psi^{(4)} & \sin y_\psi^{(4)} & 0 \\ -\sin y_\psi^{(4)} & -\cos y_\psi^{(4)} & 0 \end{bmatrix} n_z^{(4,2)} - K_6 n_z^{(4,1)},
\end{aligned} \tag{38}$$

where $K_6 = \mathrm{diag}(\begin{bmatrix} k_{61} & k_{62} \end{bmatrix})$ and $n_z^{(4,2)} = n_\nu$. The resulting residual under healthy conditions ($\varepsilon_{y_z H}^{(4,1)}$) is expressed by

$$\begin{aligned}
\varepsilon_{y_z H}^{(4,1)} &= e^{-K_6 t} \varepsilon_{zH}^{(4,1)}(0) + \int_0^t e^{-K_6(t-\mathrm{t})} \\
&\quad \left(\begin{bmatrix} \cos\psi & -\sin\psi \\ \sin\psi & \cos\psi \end{bmatrix} \begin{bmatrix} u \\ v \end{bmatrix} - \begin{bmatrix} \cos y_\psi & -\sin y_\psi \\ \sin y_\psi & \cos y_\psi \end{bmatrix} \begin{bmatrix} y_u \\ y_v \end{bmatrix} \right. \\
&\quad \left. - K_6 n_z^{(4,1)} \right) d\mathrm{t}.
\end{aligned} \tag{39}$$

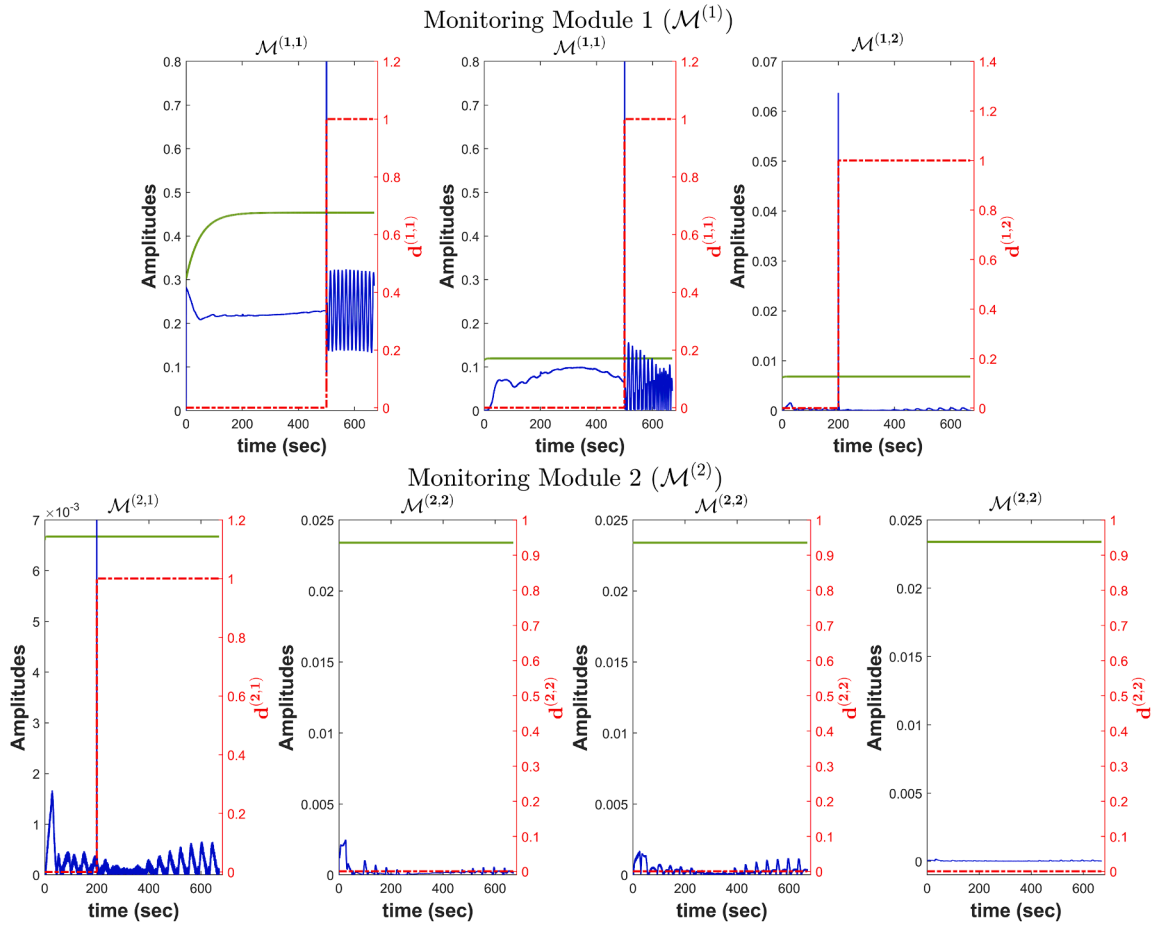

Fig. 3. Simulation results from Example 1 with the magnitude of residual signals (blue curve), the corresponding adaptive thresholds (green curve), and the decisions (dashed red curve) for the corresponding monitoring modules. (For interpretation of the references to colour in this figure legend, the reader is referred to the web version of this article.)

3.3. Combinatorial fault decision logic

In this subsection, the design of a combinatorial fault decision logic that enables the isolation of multiple sensor faults is presented. Firstly, the aggregator module receives a decision on the fault detection from the various monitoring modules based on a set of ARRs composed of residuals and adaptive thresholds. Specifically, for the monitoring module $\mathcal{M}^{(I)}$, the set of ARRs $\mathcal{E}_{y_z}^{(I)}$ is defined for detecting faults in the sensor set $S^{(I)}$, as

$$\mathcal{E}_{y_z}^{(I)} = \bigcup_j \mathcal{E}_{y_z}^{(I,j)}, \tag{40}$$

where, for $I \in \{1, \dots, 4\}$, the $j-$th ARR $\mathcal{E}_{y_z}^{(I,j)}$ is given by

$$\mathcal{E}_{y_z}^{(1,j)} : |\varepsilon_{y_z}^{(I,j)}(t)| - \bar{\varepsilon}_{y_z}^{(I,j)}(t) \leq 0, \quad j \in \{1, \dots, m_I\}. \tag{41}$$

As per the design criterion (2), a violation of the $j-$th ARR implies the occurrence of at least one sensor fault in the corresponding sensor set $S^{(I)}$. Define $T_D^{(I,j)}$ to be the first instance of violation of the $j-$th ARR $\mathcal{E}_{y_z}^{(I,j)}$ in $\mathcal{M}^{(I)}$, i.e.,

$$T_D^{(I,j)} = \begin{cases} \min\{t \in \mathbb{R}^+ : |\varepsilon_{y_z}^{(I,j)}(t)| > \bar{\varepsilon}_{y_z}^{(I,j)}(t)\}, & \neg\mathcal{E}_{y_z}^{(I,j)} \\ \infty, & \text{otherwise.} \end{cases} \tag{42}$$

Specifically, $T_D^{(I,j)}$ indicates the first instance of fault detection in the corresponding sensor within $S^{(I)}$. The output of the monitoring module $\mathcal{M}^{(I)}$ is the $I-$th decision $\mathbf{d}^{(I)}(t) = \left[\mathbf{d}^{(I,1)}(t), \quad \dots, \quad \mathbf{d}^{(I,m_I)}(t)\right]^T$, where,

$$\mathbf{d}^{(I,j)}(t) = \begin{cases} 0, & \text{if } t < T_D^{(I,j)} \\ 1, & \text{otherwise} \end{cases}. \tag{43}$$

Under the exoneration assumption (Reppa et al., 2013) which considers that $S^{(I)}$ is functioning properly before the time instant $T_{FD}^{(I)}$, $\mathbf{d}^{(I)}(t) = \mathbf{0}$ implies that no fault has occurred in the sensor set $S^{(I)}$. Upon receiving the decisions $\mathbf{d}^{(I)}(t)$ from each monitoring module in the aggregator module $\mathcal{A}$, an aggregated decision vector $\mathbf{d}(t)$ is formed by combining these individual decisions, i.e.,

$$\mathbf{d}(t) = \texttt{vcat}(\mathbf{d}^{(I)}(t)), \tag{44}$$

where `vcat()` represents a vertical concatenation function.

Remark 4. Unlike in some multi-level FDI schemes (e.g., see Reppa et al., 2013), instead of aggregating the individual sensor fault decisions $\mathbf{d}^{(I,j)}(t)$ into a boolean function, the aggregated decision vector $\mathbf{d}(t)$ composed of $\mathbf{d}^{(I,j)}(t)$ is directly used for consistency checking. Since each sensor set may have multiple sensors, such a combinatorial logic can isolate multiple sensor faults, as shown later.

The aggregator module includes the FSM, comprising zeros, ones or an '*' as its elements. Fault isolation involves conducting a consistency test between $\mathbf{d}(t)$ and the FSM, represented by F. The matrix F consists of a maximum of l rows, $l = \sum_I m_I$, with each row corresponding to

Table 2
Sensor fault signature matrix (FSM) for the designed ARRs.

	$\mathcal{F}_{c_1}$	$\mathcal{F}_{c_2}$	$\mathcal{F}_{c_3}$	$\mathcal{F}_{c_4}$	$\mathcal{F}_{c_5}$	$\mathcal{F}_{c_6}$	$\mathcal{F}_{c_7}$	$\mathcal{F}_{c_8}$	$\mathcal{F}_{c_9}$	$\mathcal{F}_{c_{10}}$	$\mathcal{F}_{c_{11}}$	$\mathcal{F}_{c_{12}}$	$\mathcal{F}_{c_{13}}$	$\mathcal{F}_{c_{14}}$	$\mathcal{F}_{c_{15}}$
$\mathcal{E}_{y_z}^{(1,1)}$	1	*	0	0	1	1	1	*	*	0	1	1	*	1	1
$\mathcal{E}_{y_z}^{(1,2)}$	0	1	0	0	1	0	0	1	1	0	1	1	1	0	1
$\mathcal{E}_{y_z}^{(2,1)}$	0	1	1	0	1	1	0	1	1	1	1	1	1	1	1
$\mathcal{E}_{y_z}^{(2,2)}$	0	0	1	0	0	1	0	1	0	1	1	0	1	1	1
$\mathcal{E}_{y_z}^{(3,1)}$	0	1	0	0	1	0	0	1	1	0	1	1	1	0	1
$\mathcal{E}_{y_z}^{(4,1)}$	1	0	*	*	1	1	1	*	*	*	1	1	*	1	1

Fig. 4. The Waterbus 2907 vessel (Courtesy: Damen Shipyards).

the j−th ARR $\mathcal{E}_{y_z}^{(I,j)}$. Further, F consists of $N_c = 2^{\mathfrak{s}} - 1$ columns, with $\mathfrak{s}$ representing the total no. of monitored sensors. Each column F_q, $q \in \{1, \dots, N_c\}$, represents a theoretical sensor fault pattern. An entry $F_{pq} = 1$ (where $p \in \{1, \dots, l\}$) indicates that at least one sensor fault within the combination $\mathcal{F}_{c_q}$ is responsible for the violation of the ARR $\mathcal{E}_{y_z}^{(I,j)}$, thereby impacting $\mathcal{S}^{(I)}$. An entry $F_{pq} =$'*' is used instead of '1' to distinguish a possible violation due to the weak sensitivity of the ARR $\mathcal{E}_{y_z}^{(I,j)}$ to a sensor fault included in $\mathcal{F}_{c_q}$. Otherwise, F_{pq} is taken to be zero. The observed fault pattern in $\mathbf{d}(t)$ is considered consistent with a theoretical pattern F_q when $\mathbf{d}_p(t) = F_{pq}$ for all $p \in \{1, \dots, l\}$.

The final diagnostic output, denoted as the diagnosis set $\mathcal{D}_s(t)$, is obtained from the aggregator module and includes all possible fault combinations $\mathcal{F}_{c_q}$ that pass the consistency test. It is important to note that, as the elements of $\mathbf{d}(t)$ can fluctuate over time, the cardinality of the diagnosis set may also change. This allows the diagnosis set to reflect the evolving fault conditions as the system operates. Given the assumption that the faults are permanent, the cardinality can only increase.

Remark 5. The selection of monitoring modules in the proposed FDI scheme should be based on the sensors that are to be monitored. Accordingly, the observer design, adaptive thresholds computation and the FSM must be updated to accommodate the new sensor configuration and additional model uncertainties.

3.4. Sensitivity analysis

While the structural sensitivity to sensor faults can be directly inferred from the residual expressions, it may be difficult to infer the weak sensitivity. A sensitivity analysis is subsequently performed to realise the smaller impacts of the faults on the residuals (and subsequently the ARRs). For the sensors considered in this work, the following sensor fault/fault combinations are possible: $\mathcal{F}_{c_1} = \{f_p\}$, $\mathcal{F}_{c_2} = \{f_\psi\}$, $\mathcal{F}_{c_3} = \{f_v\}$, $\mathcal{F}_{c_4} = \{f_\chi\}$, $\mathcal{F}_{c_5} = \{f_p, f_\psi\}$, $\mathcal{F}_{c_6} = \{f_p, f_v\}$, $\mathcal{F}_{c_7} = \{f_p, f_\chi\}$, $\mathcal{F}_{c_8} = \{f_\psi, f_v\}$, $\mathcal{F}_{c_9} = \{f_\psi, f_\chi\}$, $\mathcal{F}_{c_{10}} = \{f_v, f_\chi\}$, $\mathcal{F}_{c_{11}} = \{f_p, f_\psi, f_v\}$, $\mathcal{F}_{c_{12}} = \{f_p, f_\psi, f_\chi\}$, $\mathcal{F}_{c_{13}} = \{f_\psi, f_v, f_\chi\}$, $\mathcal{F}_{c_{14}} = \{f_v, f_\chi, f_p\}$, and $\mathcal{F}_{c_{15}} = \{f_p, f_\psi, f_v, f_\chi\}$. A Jacobian block matrix is computed for the residuals derived in Section 3 3.2. w.r.t. single faults (f_p, f_ψ, f_v and f_χ), and is given by

$$\nabla\varepsilon_{y_z}(f_z) = \begin{bmatrix} \partial\varepsilon_{y_z}^{(1,1)}(f_p) & \partial\varepsilon_{y_z}^{(1,1)}(f_\psi) & \partial\varepsilon_{y_z}^{(1,1)}(f_v) & \partial\varepsilon_{y_z}^{(1,1)}(f_\chi) \\ \partial\varepsilon_{y_z}^{(1,2)}(f_p) & \partial\varepsilon_{y_z}^{(1,2)}(f_\psi) & \partial\varepsilon_{y_z}^{(1,2)}(f_v) & \partial\varepsilon_{y_z}^{(1,2)}(f_\chi) \\ \partial\varepsilon_{y_z}^{(2,1)}(f_p) & \partial\varepsilon_{y_z}^{(2,1)}(f_\psi) & \partial\varepsilon_{y_z}^{(2,1)}(f_v) & \partial\varepsilon_{y_z}^{(2,1)}(f_\chi) \\ \partial\varepsilon_{y_z}^{(2,2)}(f_p) & \partial\varepsilon_{y_z}^{(2,2)}(f_\psi) & \partial\varepsilon_{y_z}^{(2,2)}(f_v) & \partial\varepsilon_{y_z}^{(2,2)}(f_\chi) \\ \partial\varepsilon_{y_z}^{(3,1)}(f_p) & \partial\varepsilon_{y_z}^{(3,1)}(f_\psi) & \partial\varepsilon_{y_z}^{(3,1)}(f_v) & \partial\varepsilon_{y_z}^{(3,1)}(f_\chi) \\ \partial\varepsilon_{y_z}^{(4,1)}(f_p) & \partial\varepsilon_{y_z}^{(4,1)}(f_\psi) & \partial\varepsilon_{y_z}^{(4,1)}(f_v) & \partial\varepsilon_{y_z}^{(4,1)}(f_\chi) \end{bmatrix}. \tag{45}$$

Here, each block of the matrix represents the partial derivative of the corresponding residual vector elements with respect to a sensor fault. Computing the Jacobian matrix results in

$$\nabla\varepsilon_{y_z}(f_z) = \begin{bmatrix} \mathbf{1} & \partial\varepsilon_{y_z}^{(1,1)}(f_\psi) & \mathbf{0} & \mathbf{0} \\ 0 & 1 & 0 & 0 \\ 0 & 1 & 1 & 0 \\ \mathbf{0} & \mathbf{0} & \mathbf{1} & \mathbf{0} \\ 0 & 1 & 0 & 0 \\ \mathbf{1} & \mathbf{0} & \partial\varepsilon_{y_z}^{(4,1)}(f_v) & \partial\varepsilon_{y_z}^{(4,1)}(f_\chi) \end{bmatrix}, \tag{46}$$

where $\mathbf{1}$, $\mathbf{0}$ represent an all-ones matrix and a null matrix of appropriate dimensions, respectively. The ones and zeros confirm or refute the existence of a structural relationship, respectively, whereas the following weak sensitivities are also observed:

- $\partial\varepsilon_{y_z}^{(1,1)}(f_\psi)$: A fault in the heading angle measurement enters the residual $\varepsilon_{y_z}^{(1,1)}$ directly through the heading angle estimate $\hat{\psi}^{(1)}$ and indirectly through the velocity vector estimate $\hat{v}^{(1)}$, resulting in a Jacobian given by

$$\begin{bmatrix} \frac{\hat{u}^{(1)}\sin\hat{\psi}^{(1)} + \hat{v}^{(1)}\cos\hat{\psi}^{(1)}}{|\hat{r}^{(1)}|}\left(k_{23}\mathcal{J}_1 + k_{12}\mathcal{J}_2\right) \\ \frac{\hat{u}^{(1)}\cos\hat{\psi}^{(1)} - \hat{v}^{(1)}\sin\hat{\psi}^{(1)}}{|\hat{r}^{(1)}|}\left(k_{23}\mathcal{J}_3 + k_{12}\mathcal{J}_4\right) \end{bmatrix}, \tag{47}$$

  where, $k_{12}, k_{23} \in \mathbb{R}$ are observer gains such that $K_1 = \text{diag}(\begin{bmatrix} K_{11} & k_{12} \end{bmatrix})$ and $K_2 = \text{diag}(\begin{bmatrix} k_{21} & k_{22} & k_{23} \end{bmatrix})$. Further, $\mathcal{J}_1$, $\mathcal{J}_2$, $\mathcal{J}_3$ and $\mathcal{J}_4$ represent polynomial functions of the observer's states $\hat{u}^{(1)}$, $\hat{v}^{(1)}$ and $\hat{r}^{(1)}$. By tuning the gains k_{12}, k_{23}, a balance between the fault sensitivity of the residual and observer convergence rate can be achieved. Specifically, the gains should be selected high enough to ensure fast convergence of the estimation errors but not amplify the propagation of the heading angle fault into the position residual.
- $\partial\varepsilon_{y_z}^{(4,1)}(f_v)$: The Jacobian elements are given by

$$\begin{bmatrix} -\cos(y_\chi)\cos\left(\tan^{-1}\left(\frac{y_v}{y_u}\right)\right) & -\cos(y_\chi)\sin\left(\tan^{-1}\left(\frac{y_v}{y_u}\right)\right) & 0 \\ -\sin(y_\chi)\cos\left(\tan^{-1}\left(\frac{y_v}{y_u}\right)\right) & -\sin(y_\chi)\sin\left(\tan^{-1}\left(\frac{y_v}{y_u}\right)\right) & 0 \end{bmatrix}.$$

  It can be observed that each element is bounded in the range of $[-1, 1]$, and is independent of the observer's gains. This prevents an arbitrarily large variation in the residual's value due to a fault in the velocity measurements.

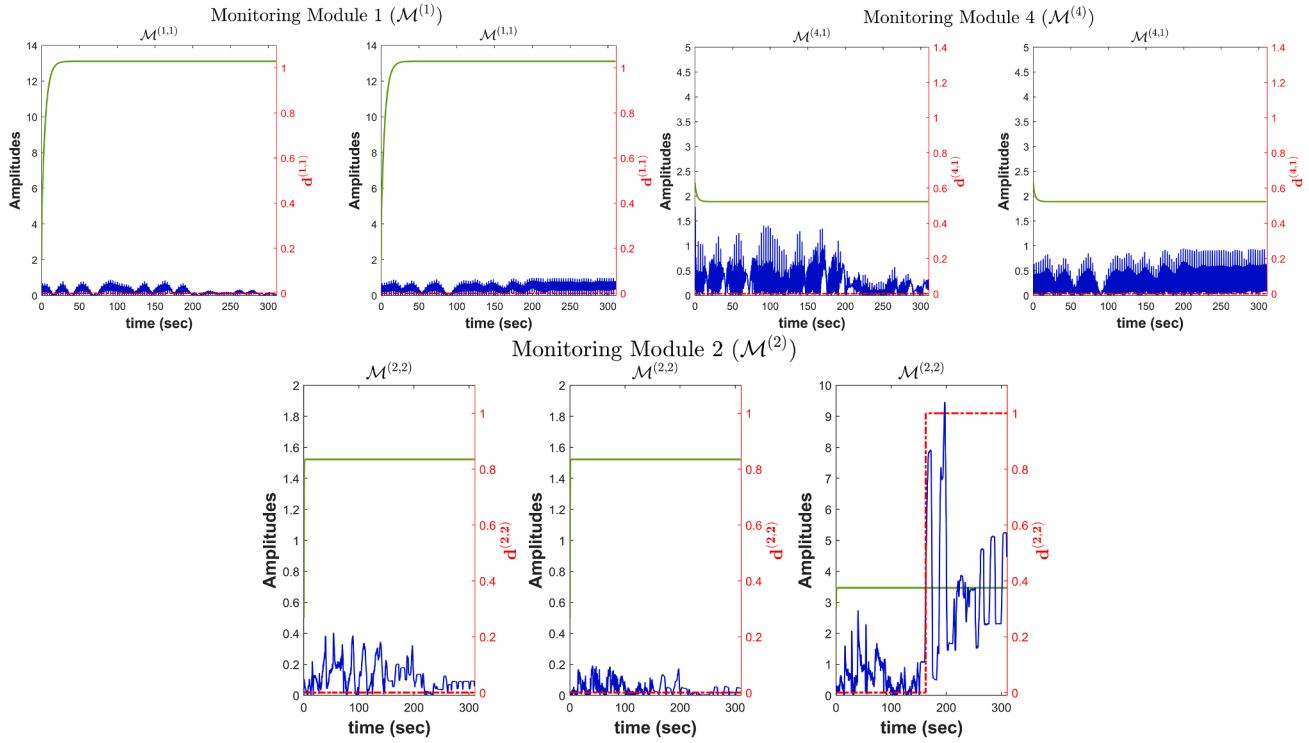

Fig. 5. Simulation results from Example 2 of the residual signals (blue curve), the corresponding adaptive thresholds (green curve), and the decisions (dashed red curve) for the corresponding monitoring modules. (For interpretation of the references to colour in this figure legend, the reader is referred to the web version of this article.)

- $\partial\varepsilon_{y_z}^{(4,1)}(f_\chi)$: The Jacobian elements are given by

$$\begin{bmatrix} U_y \sin(y_\chi) \\ -U_y \cos(y_\chi) \end{bmatrix}, \tag{48}$$

where $U_y = \sqrt{y_u^2 + y_v^2}$. The weak sensitivity of $\varepsilon_{y_z}^{(4,1)}$ to faults in course angle measurements is attributed to the faults appearing in the domain of sine and cosine functions, which return values in a small range $[-1, 1]$. When multiplied by the ship's measured speed U_y, a bounded sensitivity in the $[-U_y, U_y]$ range is obtained. Therefore, the sensitivities are small at low speeds, however, it is non-negligible at higher speeds.

Based on the above sensitivity analysis results, the FSM for the ARRs designed in this work is determined and is given in Table 2. The weak sensitivity of an ARR to sensor fault(s) is denoted by a '*' symbol.

4. Simulation results

The proposed FDI scheme is further verified in this section using simulation examples that involve two different vessel types: a pusher-barge inland vessel and a catamaran-type ferry.

4.1. Example 1: TPQR pusher-barge system

This section presents simulation results for an 11BP pusher-barge system as studied in Koh and Yasukawa (2012). The vessel has full-scale dimensions and is modified to have a twin-propeller and quad rudder (TPQR) actuator configuration for improved maneuverability. Its MMG model parameters, including the hydrodynamic coefficients, are provided in Koh and Yasukawa (2012), Zhang et al. (2024a).

The vessel is simulated to follow a predefined path in an inland waterway, emulating the practical conditions in a canal with medium-shallow water. Wind conditions are modelled with a velocity of $V = 17$ m/s, corresponding to a value of 7 in the Beaufort scale, and at an angle of $\beta_V = 45°$, coming from the southwest direction. Additionally, the total forward resistance, including the effects of shallow water, is modelled by considering a water depth-to-draft ratio of 1.5. Therefore, the magnitude of the unknown force vector τ_d is equal to $|\tau_d| = (|\tau_w| + |\tau_H|) \leq \bar{\tau}_d$. Three sensors, namely the GNSS, gyrocompass and IMU, are considered on the vessel. Each sensor is assumed to be corrupted by Gaussian white noise having an amplitude within 3 % of the mean absolute value of the noiseless sensor measurement.

For residual generation, the sensor sets $\mathcal{S}^{(1)}$ and $\mathcal{S}^{(2)}$ are considered, with $\mathcal{S}^{(1)}$ containing the GNSS and gyrocompass and $\mathcal{S}^{(2)}$

Table 3
Parameters for designing the adaptive thresholds for each residual.

Example 1	
Parameters	Values
$\rho^{(1,1)}, \rho^{(1,2)}, \rho^{(2,1)}, \rho_d^{(1,1)}, \rho_d^{(1,2)}, \rho_d^{(2,1)}$	0.01
$\xi^{(1,1)}, \xi^{(1,2)}, \xi^{(2,1)}, \xi_d^{(1,1)}, \xi_d^{(1,2)}, \xi_d^{(2,1)}$	0.3
$\rho^{(2,2)}, \rho_d^{(2,2)}$	0.0001
$\xi^{(2,2)}, \xi_d^{(2,2)}$	45
Example 2	
Parameters	Values
$\rho^{(1,1)}, \rho^{(2,2)}$	1
$\rho_d^{(1,1)}, \rho_d^{(2,2)}$	10
$\rho_d^{(2,2)}$ [a] $*$	5
$\xi^{(1,1)}$	1
$\xi_d^{(1,1)}$	9
$\xi^{(2,2)}, \xi_d^{(2,2)}$	5
$\rho^{(4,1)}$	0.01
$\rho_d^{(4,1)}$	1
$\xi^{(4,1)}$	0.3
$\xi_d^{(4,1)}$	0.9

[a] Corresponding to yaw-rate measurement.

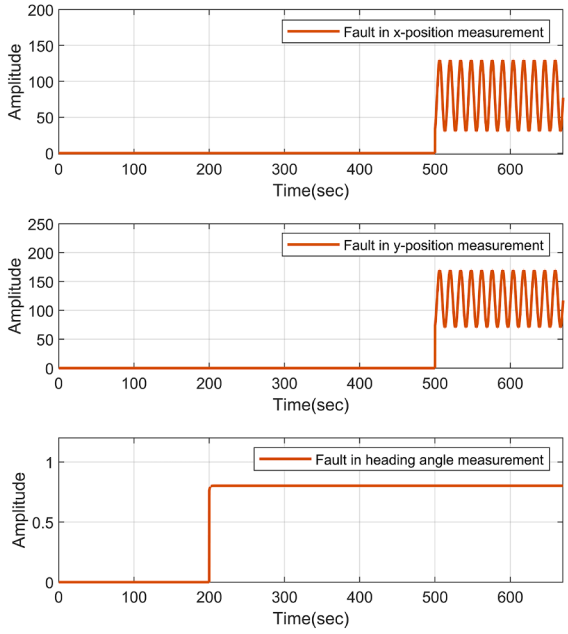

(a) The GNSS and gyrocompass faults in Example 1 (Equation (49)).

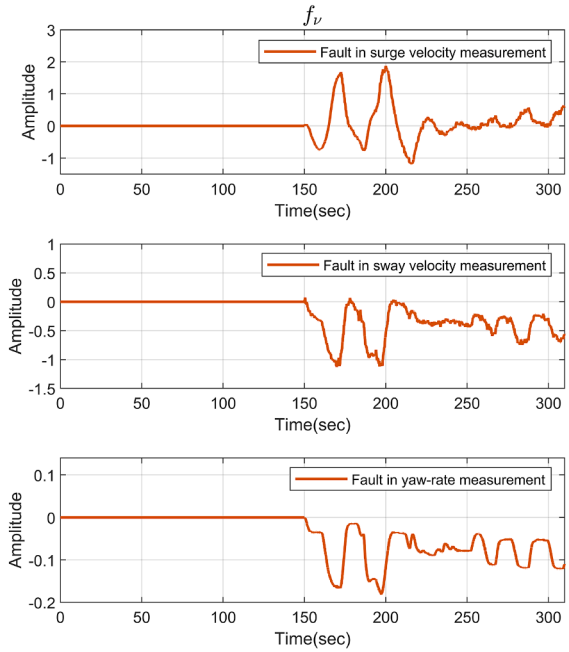

(b) The IMU fault in Example 2 (Equation (50)).

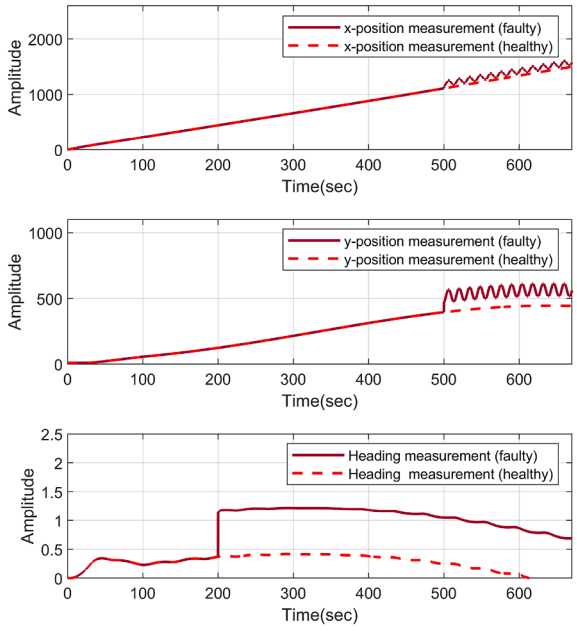

(c) The healthy and faulty sensor measurements in Example 1.

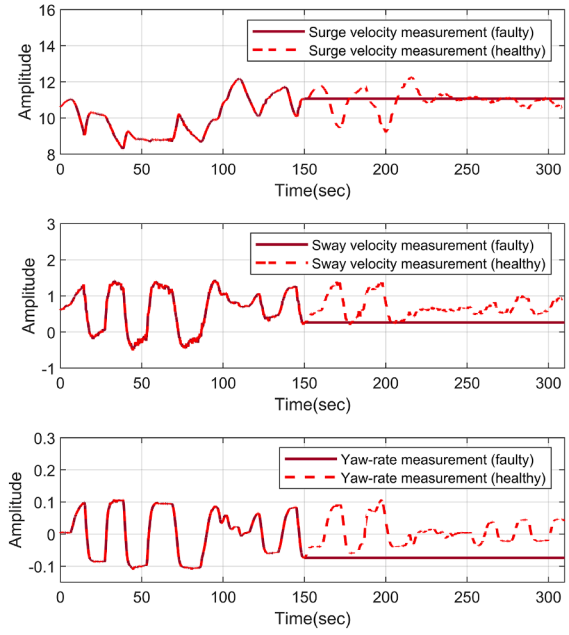

(d) The healthy and faulty sensor measurements in Example 2.

Fig. 6. Visualisation of the fault functions and the resulting measurements corresponding to Examples 1 and 2.

containing the gyrocompass and IMU. Two monitoring modules $\mathcal{M}^{(I)}, I \in \{1,2\}$, are subsequently designed, based on the measurements obtained from the corresponding sensor sets, the input force vector, and using ARRs as given by Equation (41). The fault detection observer gain matrices K_1, K_2, K_4 are taken to be equal to a diagonal matrix diag($\begin{bmatrix}100, & 100, & 100\end{bmatrix}$), and k_3 is equal to 100. Further, the design parameters for the adaptive thresholds in each monitoring module are given in Table 3. The theoretical fault signatures used in the aggregator module are provided in Table 4, where, $\mathcal{F}_{c_1} = \{f_p\}$, $\mathcal{F}_{c_2} = \{f_\psi\}$, $\mathcal{F}_{c_3} = \{f_v\}$, $\mathcal{F}_{c_4} = \{f_p, f_\psi\}$, $\mathcal{F}_{c_5} = \{f_p, f_v\}$, $\mathcal{F}_{c_6} = \{f_\psi, f_v\}$ and $\mathcal{F}_{c_7} = \{f_p, f_\psi, f_v\}$. An edge case is observed when the aggregated decision vector $\mathbf{d}(t) = \begin{bmatrix}0 & 1 & 1 & 1\end{bmatrix}^T$ is obtained. The resulting diagnosis set

Table 4
Example 1 - Sensor fault signature matrix for the aggregator $\mathcal{A}$.

	$\mathcal{F}_{c_1}$	$\mathcal{F}_{c_2}$	$\mathcal{F}_{c_3}$	$\mathcal{F}_{c_4}$	$\mathcal{F}_{c_5}$	$\mathcal{F}_{c_6}$	$\mathcal{F}_{c_7}$
$\mathcal{E}_{y_z}^{(1,1)}$	1	*	0	1	1	*	1
$\mathcal{E}_{y_z}^{(1,2)}$	0	1	0	1	0	1	1
$\mathcal{E}_{y_z}^{(2,1)}$	0	1	1	1	1	1	1
$\mathcal{E}_{y_z}^{(2,2)}$	0	0	1	0	1	1	1

is equal to $\mathcal{D}_s(t) = \{\mathcal{F}_{c_6}, \mathcal{F}_{c_7}\}$, implying that the faults f_ψ, f_v have occurred, and that the fault f_p may or may not have occurred. This ambiguity is eliminated when $\mathbf{d}(t) = \begin{bmatrix}1 & 1 & 1 & 1\end{bmatrix}^T$, leading to $\mathcal{D}_s(t) = \mathcal{F}_{c_7}$, thereby isolating all the occurred faults.

A fault scenario is simulated to further verify the proposed FDI method. The simulation is carried out for a total duration of 670 s. Permanent faults in the gyrocompass and GNSS sensors are considered to have occurred at $T_{f_\psi} = 200$ secs and $T_{f_p} = 500$ secs, respectively. The respective fault functions are given by

$$f_\psi = \mathfrak{u}(t - T_{f_\psi})(\mathfrak{a}_{f_\psi} + (1 - e^{-(t - T_{f_\psi})})) \tag{49}$$

$$f_p = \mathfrak{u}(t - T_{f_p})(\mathfrak{a}_{f_p} + \sin(0.45t)), \tag{50}$$

where $\mathfrak{u}(t)$ denotes a unit step function, and $\mathfrak{a}_{f_\psi}, \mathfrak{a}_{f_p}$ are fault amplitudes ranging between $1-2$ times the mean absolute values of the noiseless sensor measurement. The time plots of the fault functions and the respective sensor measurements (under healthy and faulty conditions) are shown in Figs. 6(a) and 6(c), respectively. The resulting residual signals and the corresponding adaptive thresholds for the j^{th} sensor monitored by $\mathcal{M}^{(I)}$ are plotted under $\mathcal{M}^{(I,j)}$ in Fig. 3. As shown, the residuals corresponding to the gyrocompass (in $\mathcal{M}^{(1,2)}$ and $\mathcal{M}^{(2,1)}$), the residuals corresponding to the GNSS (in $\mathcal{M}^{(1,1)}$) exceed the respective thresholds. The fault detection time, which is expressed by (42), is equal to $T_D^{(1,1)} = 500.1$ secs, $T_D^{(1,2)} = 200$ secs and $T_D^{(2,1)} = 200.1$ secs, respectively.

For $t < 200$ secs, the aggregated decision vector $\mathbf{d}(t)$'s elements remain zero, and the diagnosis set corresponds to a null set. For $200 \le t < 500$ secs, the occurrence of the first fault is detected by the residual exceeding the adaptive threshold, resulting in $\mathbf{d}(t) = \begin{bmatrix}0 & 1 & 1 & 0\end{bmatrix}^T$. For $t \ge 500$ secs, the second fault is detected, leading to $\mathbf{d}(t) = \begin{bmatrix}1 & 1 & 1 & 0\end{bmatrix}$. At the end of the simulation, a consistency test is performed by comparing the observed pattern $\mathbf{d}(t)$ to the theoretical patterns $\mathcal{F}_{c_q}$, which results in a diagnosis set $\mathcal{D}_s(t) = \{\mathcal{F}_{c_2}, \mathcal{F}_{c_4}\} = \{\{f_\psi\}, \{f_p, f_\psi\}\}$, thereby isolating the faulty sensors.

4.2. Example 2: Damen Waterbus 2907 shuttle

In this section, an example of a catamaran-type passenger ferry is considered to showcase and verify the design of the proposed FDI scheme. The vessel, namely, the Waterbus 2907, is a fully electric water shuttle designed by Damen Shipyards (Damen Shipyards Group, 2025), equipped with two azimuth thrusters and two bow thrusters (see Fig. 4). The vessel's maneuvering model is identified using logged data, which includes sensor measurements from onboard GNSS/INS and the propulsion system in various maneuvers performed on the Merwede River. The dynamical model of the vessel and the actuation forces can be expressed using equations (7), (9), and (15), respectively, and its main parameters are mentioned in Table 5. For this example, the unknown added force vector is modelled as $\tau_d = \tau_w$, and the wind conditions are considered the same as in Example 1.

The vessel is equipped with an IMU and uses dual GNSS antennas instead of a gyrocompass for heading angle estimation. The fault combinations are given as $\mathcal{F}_{c_1} = \{f_p\}$, $\mathcal{F}_{c_2} = \{f_v\}$, $\mathcal{F}_{c_3} = \{f_\chi\}$, $\mathcal{F}_{c_4} = \{f_p, f_v\}$, $\mathcal{F}_{c_5} = \{f_p, f_\chi\}$, $\mathcal{F}_{c_6} = \{f_v, f_\chi\}$, and $\mathcal{F}_{c_7} = \{f_p, f_v, f_\chi\}$. Furthermore, three residuals are considered, resulting in a fault signature matrix as shown in Table 6. The observer gain matrices are given by the diagonal matrices $K_1 = \text{diag}(\begin{bmatrix}10 & 10\end{bmatrix})$, $K_4 = \text{diag}(\begin{bmatrix}10 & 5 & 5\end{bmatrix})$, and $K_6 = \text{diag}(\begin{bmatrix}2 & 10\end{bmatrix})$, respectively. The design parameters for the adaptive thresholds are given in Table 3.

Table 5
Main parameters of the Damen waterbus 2907 shuttle.

Parameter	Description	Value	Unit
L_{oa}	Overall length	28.65	m
b	Beam	7.50	m
m	Mass	45000	kg
x_R	Thruster's x-coordinate	-12	m
y_R	Thruster's y-coordinate	± 3.175	m

Table 6
Example 2 - Sensor fault signature matrix for the aggregator $\mathcal{A}$.

	$\mathcal{F}_{c_1}$	$\mathcal{F}_{c_2}$	$\mathcal{F}_{c_3}$	$\mathcal{F}_{c_4}$	$\mathcal{F}_{c_5}$	$\mathcal{F}_{c_6}$	$\mathcal{F}_{c_7}$
$\mathcal{E}_{y_z}^{(1,1)}$	1	0	0	1	1	0	1
$\mathcal{E}_{y_z}^{(2,2)}$	0	1	0	1	0	1	1
$\mathcal{E}_{y_z}^{(4,1)}$	1	*	*	1	1	*	1

The vessel is simulated to perform various maneuvers, including zigzag and turning, for a duration of 310 secs. A *sensor disconnection* fault is considered, which causes new sensor measurements to be lost, with static measurements received in their place. Such a fault can occur due to an Ethernet failure and can be difficult to distinguish from a stationary or stopping vessel Conejo et al. (2025). In this example, a sensor disconnection fault affecting the velocity measurements is simulated at time $T_{f_v} = 150$ secs, with the fault evolution function given by

$$\begin{matrix} f_v(t) = 0 \text{if } t < T_{f_v} \\ v(T_{f_v}) - v(t) \text{if } t \ge T_{f_v}. \end{matrix} \tag{51}$$

Fig. 6(b) shows the time plot of the above fault function. Its impact on the sensor measurements is visualised in Fig. 6(d). The obtained diagnosis results, including the residual signals, adaptive thresholds, and decisions, are shown in Fig. 5. The fault detection time, which is equal to the instance of violation of the ARR $\mathcal{E}_{y_z}^{(2,2)}$, is given by $T_D^{(2,2)} = 163$ secs and results in an aggregated decision vector equal to $\mathbf{d}(t) = \begin{bmatrix}0 & 1 & 0\end{bmatrix}^T$. Ultimately, the outcome of the consistency test is a diagnosis set $\mathcal{D}_s(t) = \{\mathcal{F}_{c_2}, \mathcal{F}_{c_6}\} = \{\{f_v\}, \{f_v, f_\chi\}\}$, which leads to the isolation of the faulty IMU sensor. Therefore, the faulty IMU sensor is isolated, whereas a possible fault f_χ is indicated.

5. Conclusions and future research

This paper presents an observer-based FDI scheme for diagnosing multiple faults in the navigational sensors of an ASV. The proposed scheme effectively addresses challenges associated with modelling complexities, variations in sensor and actuator configurations, and environmental disturbances impacting the ASV. By employing a bank of monitoring modules with structurally sensitive residuals tailored to different vessel dynamics and sensor measurement models, the scheme can diagnose multiple sensor faults. Furthermore, an aggregator module is designed, which is equipped with a combinatorial fault decision logic, enabling the isolation of faulty sensors. Adaptive thresholds are also derived for residual bounding, which helps eliminate false positives and improve diagnostic reliability. Extensive simulations with two different vessel types and sensor setups verify the effectiveness of the proposed scheme, demonstrating that the faults can be isolated across various scenarios.

For future research, observer design incorporating adaptive approximation of environmental disturbances is proposed to further enhance fault detectability. In addition, various fault signature matrices are proposed to account for factors such as the sequence of fault occurrences, signs of residual violation, and sensitivities, for improved fault isolation. Validation of the proposed FDI scheme in open sea conditions under

waves and tidal currents is also a crucial step towards practical deployment and is also proposed for future work.

CRediT authorship contribution statement

Abhishek Dhyani: Writing – review & editing, Writing – original draft, Visualization, Validation, Software, Project administration, Methodology, Investigation, Formal analysis, Data curation, Conceptualization; **Kasper van der El:** Writing – review & editing, Supervision; **Rudy R. Negenborn:** Writing – review & editing, Supervision, Project administration, Funding acquisition; **Vasso Reppa:** Writing – review & editing, Supervision, Project administration, Funding acquisition, Conceptualization.

Declaration of competing interest

The authors declare that they have no known competing financial interests or personal relationships that could have appeared to influence the work reported in this paper.

Appendix A. External forces and moments

In this work, two types of external/environmental forces and moments acting on the vessel are considered: 1) forces due to wind and 2) hydrodynamic forces acting on the vessel's hull, including the forces due to the shallow-water effect.

A.1. Wind forces

The effect of wind forces acting on the vessel can be modelled by using the following expression, under the assumption that the ship is symmetrical about the $x_p z_p$ and $y_p z_p$ planes (Fossen, 2011)

$$\tau_w = \begin{bmatrix} X_W \\ Y_W \\ N_W \end{bmatrix} = \frac{1}{2} P_a V_r^2 \begin{bmatrix} -c_x \cos(\gamma_r) A_F \\ c_y \sin(\gamma_r) A_L \\ c_n \sin(2\gamma_r) A_L L_{oa} \end{bmatrix}, \tag{A.1}$$

where

$$\begin{aligned} V_r &= \sqrt{u_r^2 + v_r^2} \\ \gamma_r &= -\text{atan2}(v_r, u_r). \end{aligned} \tag{A.2}$$

Here, atan2 is a 2-argument inverse tangent function. The notation P_a denotes the air density; V_r is the relative wind speed; γ_r the relative wind angle of attack; c_x, c_y and c_n the wind coefficients for the horizontal plane motions; A_F, A_L the frontal and lateral projected areas of the vessel above the water, respectively; L_{oa} the overall length of the vessel. u_r and v_r are the relative velocity components of V_r in the x_p and y_p directions, such that

$$\begin{aligned} u_r &= u - V\cos(\beta_V - \psi) \\ v_r &= v - V\sin(\beta_V - \psi). \end{aligned} \tag{A.3}$$

The wind speed $V \in \mathbb{R}$ and direction $\beta_V \in \mathbb{R}$ can be measured in real-time by an anemometer and a weather vane, respectively. Furthermore, the coefficients c_x, c_y, and c_n can be empirically calculated (Fossen, 2011). In this work, the wind forces acting on the vessel are treated as unknown.

A.2. Hull forces

While the Abkowitz model (Equation (9)) considers the hydrodynamic forces and moments acting on the vessel's hull as part of the known nonlinear dynamics, in this work, these forces are considered unknown for the MMG model. The vector $\tau_H = \begin{bmatrix} X_H & Y_H & N_H \end{bmatrix}^T$ represents these forces and moments and forms a part of the unknown force vector τ_d for Equation (13). For inland waterway vessels, this includes the resistance due to the shallow-water effect, which is a predominant factor impacting the vessel's motion. The generalised hydrodynamic forces acting on the vessel hull are formulated as:

$$\begin{aligned} X_H &= 0.5\rho L_{\text{oa}} T U^2 X'_H \\ Y_H &= 0.5\rho L_{\text{oa}} T U^2 Y'_H \\ N_H &= 0.5\rho L_{\text{oa}}^2 T U^2 N'_H, \end{aligned} \tag{A.4}$$

where ρ is defined as the density of freshwater, U is the vessel's speed, and T is the vessel's draught. X'_H, Y'_H and N'_H are dimensionless quantities given by

$$\begin{aligned} X'_H =& -R'_0 \cos^2\beta_m + X'_{\beta\beta}\beta_m^2 + X'_{\beta r}\beta_m r' + X'_{rr} r'^2 \\ &+ X'_{\beta\beta\beta\beta}\beta_m^4 \\ Y'_H =& Y'_\beta \beta_m + Y'_r r' + Y'_{\beta\beta\beta}\beta_m^3 + Y'_{\beta\beta r}\beta_m^2 r' + Y'_{\beta rr}\beta_m r'^2 \\ &+ Y'_{rrr} r'^3 \\ N'_H =& N'_\beta \beta_m + N'_r r' + N'_{\beta\beta\beta}\beta_m^3 + N'_{\beta\beta r}\beta_m^2 r' + N'_{\beta rr}\beta_m r'^2 \\ &+ N'_{rrr} r'^3, \end{aligned} \tag{A.5}$$

where $X'_{\beta\beta}, X'_{\beta r}, \ldots, N'_{rrr}$ are the hydrodynamic derivatives in the MMG modelling approach, β_m is the midship drift angle, and r' is the non-dimensional yaw rate which is equal to rL_{oa}/U. The expression for the resistance coefficient, R'_0, modified to include the impact of shallow water effect on the vessel, is given by Zhang et al. (2025):

$$\begin{aligned} R'_0 &= \frac{R_{\text{Sh}}}{\left(0.5\rho L_{\text{oa}} T U^2\right)} \\ R_{\text{Sh}} &= 0.5\rho S_W U^2 \left(C_F \left(1 + \left(k + \bar{k}\right)\right) + C_W\right), \end{aligned} \tag{A.6}$$

where, S_W represents the ship's wetted surface area; C_F, C_W are the frictional resistance and the wave-making resistance coefficients, k is the ship's form factor in deep water and $\bar{k}$ is the additional viscous resistance in shallow water.

Appendix B. Adaptive thresholds computation

B.1. Monitoring module $\mathcal{M}^{(1)}$

A bound on $|\varepsilon_{zH}^{(1)}|$ satisfies the inequality

$$\begin{aligned} |\varepsilon_{zH}^{(1)}| \leq & \begin{bmatrix} |e^{-K_1 t}| & \mathbf{0} \\ \mathbf{0} & |e^{-K_2 t}| \end{bmatrix} \begin{bmatrix} |\varepsilon_{zH}^{(1,1)}(0)| \\ |\varepsilon_{zH}^{(1,2)}(0)| \\ |\varepsilon_{zH}^{(1,3)}(0)| \end{bmatrix} \\ &+ \int_0^t \left(\begin{bmatrix} |e^{-K_1(t-\mathrm{t})}| & \mathbf{0} \\ \mathbf{0} & |e^{-K_2(t-\mathrm{t})}| \end{bmatrix} \begin{bmatrix} |\tilde{\gamma}_{1H}^{(1)}(\mathrm{t})| \\ |\tilde{\gamma}_{2H}^{(1)}(\mathrm{t})| + |\Delta(\eta,\nu)| + \\ |-K_2 R^T(\hat{\psi}_H^{(1)}(\mathrm{t}))n_\eta| + |-K_2(R^T(\hat{\psi}_H^{(1)}(\mathrm{t}))\eta(\mathrm{t}) - \nu(\mathrm{t}))| \end{bmatrix} \right. \\ &\left. + \begin{bmatrix} |-K_1 e^{-K_1(t-\mathrm{t})}| & \mathbf{0} \\ \mathbf{0} & |-K_2 e^{-K_2(t-\mathrm{t})}| \end{bmatrix} \begin{bmatrix} |n_\eta| \\ \mathbf{0} \end{bmatrix} \right) d\mathrm{t}. \end{aligned} \tag{B.1}$$

Based on the Assumption 3, a bound on each term constituting the inequality (B.1) is determined and is given by

1. $\begin{bmatrix} |\varepsilon_{zH}^{(1,1)}(0)| & \\ |\varepsilon_{zH}^{(1,2)}(0)| & |\varepsilon_{zH}^{(1,3)}(0)| \end{bmatrix}^T = \begin{bmatrix} \bar{p}^{(1)} & \bar{\psi}^{(1)} & \bar{v}^{(1)} \end{bmatrix}^T = \bar{z}^{(1)T},$
2. $\begin{bmatrix} |e^{-K_1 t}| & \mathbf{0} \\ \mathbf{0} & |e^{-K_2 t}| \end{bmatrix} \leq \rho^{(1)} e^{-\xi^{(1)} t} = \Phi^{(1)}(t),$
3. $\begin{bmatrix} |-K_1 e^{-K_1 t}| & \mathbf{0} \\ \mathbf{0} & |-K_2 e^{-K_2 t}| \end{bmatrix} \leq \rho_d^{(1)} e^{-\xi_d^{(1)} t},$
4. $|n_\eta| \leq \begin{bmatrix} \bar{n}_z^{(1,1)} & \bar{n}_z^{(1,2)} \end{bmatrix}^T,$
5. $|\tilde{\gamma}_{1H}^{(1)}| = |R(\psi)\nu - R(\hat{\psi}_H^{(1)})\hat{\nu}_H^{(1)}| \leq \lambda_{\gamma_1^{(1)}} \begin{bmatrix} |\varepsilon_{zH}^{(1,1)}| & |\varepsilon_{zH}^{(1,2)}| \end{bmatrix}^T,$

$|\tilde{\gamma}_{2H}^{(1)}| = |f(v,\tau) - f(\hat{v}_H^{(1)},\tau)| \le \lambda_{\gamma_2^{(1)}} |\varepsilon_{zH}^{(1,3)}|$,
$|\Delta(\eta,\nu)| = \tilde{\tau}_d \le \bar{\tilde{\tau}}_d$, and,

6. $|-K_2 R^T(\hat{\psi}_H^{(1)}) n_\eta| \le \begin{bmatrix} k_{21}(\bar{n}_{z_1}^{(1,1)} + \bar{n}_{z_2}^{(1,1)}) \\ k_{22}(\bar{n}_{z_1}^{(1,1)} + \bar{n}_{z_2}^{(1,1)}) \\ k_{23}(\bar{n}_z^{(1,2)}) \end{bmatrix} = \bar{\tilde{n}}_\eta$,
$|-K_2(R^T(\hat{\psi}_H^{(1)})\eta - \nu)| \le (\tilde{\eta} - \tilde{\nu})$, with,
$|-K_2 R^T(\hat{\psi}_H)\eta| \le$
$\begin{bmatrix} k_{21}(\bar{x}_p + \bar{y}_p) & k_{22}(\bar{x}_p + \bar{y}_p) & k_{23}(\bar{\psi}) \end{bmatrix}^T = \tilde{\eta}$,
$|K_2 \nu| \in [\tilde{\nu}, \bar{\tilde{\nu}}]$, $\eta \in [\underline{\eta}, \bar{\eta}] \in \left[\begin{bmatrix} \underline{x} & \underline{y} & \underline{\psi} \end{bmatrix}^T, \begin{bmatrix} \bar{x} & \bar{y} & \bar{\psi} \end{bmatrix}^T \right]$,

and where, $\lambda_{\gamma_1^{(1)}}, \lambda_{\gamma_2^{(1)}}$ are the respective Lipschitz constants. Upon substituting the above equations into (B.1), the state estimation error under healthy conditions $\varepsilon_{zH}^{(1)}$ satisfies

$$|\varepsilon_{zH}^{(1)}| \le \Phi^{(1)}(t) \begin{bmatrix} \bar{p}^{(1)} \\ \bar{\psi}^{(1)} \\ \bar{v}^{(1)} \end{bmatrix} + \int_0^t \left(\rho_d^{(1)} e^{-\xi_d^{(1)}(t-\mathfrak{t})} \begin{bmatrix} \bar{n}_z^{(1,1)} \\ \bar{n}_z^{(1,2)} \\ \mathbf{0} \end{bmatrix} + \Phi^{(1)}(t-\mathfrak{t}) \begin{bmatrix} \lambda_{\gamma_1^{(1)}} |\varepsilon_{zH}^{(1,1)}(\mathfrak{t})| \\ \lambda_{\gamma_1^{(1)}} |\varepsilon_{zH}^{(1,2)}(\mathfrak{t})| \\ \lambda_{\gamma_2^{(1)}} |\varepsilon_{zH}^{(1,3)}(\mathfrak{t})| + \bar{\tilde{\tau}}_d + \bar{\tilde{n}}_\eta + (\tilde{\eta} - \tilde{\nu}) \end{bmatrix} \right) d\mathfrak{t}. \tag{B.2}$$

Applying the Bellman-Gronwall lemma to Equation (B.2) and by using the relation in (30), the $j-$th component of the adaptive threshold ($j \in \{1,2\}$) for the sensor faults in $\mathcal{S}^{(1)}$ can be expressed as Reppa et al. (2016)

$$\bar{\varepsilon}_{y_z}^{(1,j)}(t) = E^{(1,j)}(t) + \rho^{(1,j)} \Lambda_1 \int_0^t Z^{(1,j)}(\mathfrak{t}) e^{-\xi^{(1,j)}(t-\mathfrak{t})} d\mathfrak{t} + \bar{n}_z^{(1,j)}, \tag{B.3}$$

where

$$E^{(1)}(t) = \rho^{(1)} e^{-\xi^{(1)} t} \bar{z}^{(1)} + \frac{\rho_d^{(1)} \bar{n}_z^{(1)}}{\xi_d^{(1)}} (1 - e^{-\xi_d^{(1)} t}) + \int_0^t \rho^{(1)} e^{-\xi^{(1)}(t-\mathfrak{t})} \begin{bmatrix} \mathbf{0} \\ \bar{\tilde{\tau}}_d + \bar{\tilde{n}}_\eta + (\tilde{\eta} - \tilde{\nu}) \end{bmatrix} d\mathfrak{t} \tag{B.4}$$

$$Z^{(1)}(t) = E^{(1)}(t) + \rho^{(1)} \Lambda_1 \int_0^t E^{(1)}(\mathfrak{t}) e^{(\rho^{(1)}\Lambda_1 - \xi^{(1)})(t-\mathfrak{t})} d\mathfrak{t}.$$

B.2. Monitoring module $\mathcal{M}^{(2)}$

Similar to Equation (B.2), a bound on the magnitude of the state estimation error under healthy conditions $|\varepsilon_{zH}^{(2)}|$ is computed and is given by

$$|\varepsilon_{zH}^{(2)}| \le \Phi^{(2)}(t) \begin{bmatrix} \bar{\psi}^{(2)} \\ \bar{v}^{(2)} \end{bmatrix} + \int_0^t \left(\Phi^{(2)}(t-\mathfrak{t}) \begin{bmatrix} \lambda_{\gamma_1^{(2)}} |\varepsilon_{zH}^{(2,1)}(\mathfrak{t})| \\ \lambda_{\gamma_2^{(2)}} |\varepsilon_{zH}^{(2,2)}(\mathfrak{t})| + \bar{\tilde{\tau}}_d \end{bmatrix} + \rho_d^{(2)} e^{-\xi_d^{(2)}(t-\mathfrak{t})} \begin{bmatrix} \bar{n}_z^{(2,1)} \\ \bar{n}_z^{(2,2)} \end{bmatrix} \right) d\mathfrak{t}, \tag{B.5}$$

where,

1. $\begin{bmatrix} |\varepsilon_{zH}^{(2,1)}(0)| & |\varepsilon_{zH}^{(2,2)}(0)| \end{bmatrix}^T = \begin{bmatrix} \bar{\psi}^{(2)} & \bar{v}^{(2)} \end{bmatrix}^T = \bar{z}^{(2)T}$,
2. $\begin{bmatrix} |e^{-k_3 t}| & \mathbf{0} \\ \mathbf{0} & |e^{-K_4 t}| \end{bmatrix} \le \rho^{(2)} e^{-\xi^{(2)} t} = \Phi^{(2)}(t)$,
3. $\begin{bmatrix} |-k_3 e^{-k_3 t}| & \mathbf{0} \\ \mathbf{0} & |-K_4 e^{-K_4 t}| \end{bmatrix} \le \rho_d^{(2)} e^{-\xi_d^{(2)} t}$,
4. $\begin{bmatrix} |n_z^{(2,1)}| & |n_z^{(2,2)}| \end{bmatrix}^T \le \begin{bmatrix} \bar{n}_z^{(2,1)} & \bar{n}_z^{(2,2)} \end{bmatrix}^T$,
5. $|r - \hat{r}_H^{(2)}| = |\tilde{\gamma}_{1H}^{(2)}| \le \lambda_{\gamma_1^{(2)}} |\varepsilon_{zH}^{(2,1)}|$, $|f(v,\tau) - f(\hat{v}_H^{(2)},\tau)| = |\tilde{\gamma}_{2H}^{(2)}| \le \lambda_{\gamma_2^{(2)}} |\varepsilon_{zH}^{(2,2)}|$, $|\Delta(\eta,\nu)| = \tilde{\tau}_d \le \bar{\tilde{\tau}}_d$,

where, $\lambda_{\gamma_1^{(2)}}$ and $\lambda_{\gamma_2^{(2)}}$ are the respective Lipschitz constants. Further, let us define $\rho^{(I,j)}$, $\xi^{(I,j)}$, $\rho_d^{(I,j)}$, $\xi_d^{(I,j)}$ as positive constants satisfying $|e^{-K_p t}| \le \rho^{(I)} e^{-\xi^{(I)} t}$ and $\xi^{(I)} > \Lambda_I \rho^{(I)}$, $p \in \{1,\dots,4\}$; $\Lambda_1 = \lambda_{\gamma_1^{(1)}}$, $\Lambda_2 = \begin{bmatrix} \lambda_{\gamma_1^{(2)}} & \mathbf{0} \\ \mathbf{0} & \lambda_{\gamma_2^{(2)}} + \lambda_{\bar{\tilde{\tau}}_d} \end{bmatrix}$.

Applying the Bellman-Gronwall lemma to Equation (B.5) and by using the relation in (30), for the faults occurring in the sensor set $\mathcal{S}^{(2)}$, the $j-$th adaptive threshold ($j \in \{1,2\}$) is expressed as

$$\bar{\varepsilon}_{y_z}^{(2,j)}(t) = E^{(2,j)}(t) + \rho^{(2,j)} \Lambda_2^{(j)} \int_0^t Z^{(2,j)}(\mathfrak{t}) e^{-\xi^{(2,j)}(t-\mathfrak{t})} d\mathfrak{t} + \bar{n}_z^{(2,j)}, \tag{B.6}$$

where

$$E^{(2)}(t) = \rho^{(2)} e^{-\xi^{(2)} t} \bar{z}^{(2)} + \frac{\rho_d^{(2)} \bar{n}_z^{(2)}}{\xi_d^{(2)}} (1 - e^{-\xi_d^{(2)} t}) + \int_0^t \rho^{(2)} e^{-\xi^{(2)}(t-\mathfrak{t})} \begin{bmatrix} 0 \\ \bar{\tilde{\tau}}_d \end{bmatrix} d\mathfrak{t} \tag{B.7}$$

$$Z^{(2)}(t) = E^{(2)}(t) + \rho^{(2)} \Lambda_2 \int_0^t E^{(2)}(\mathfrak{t}) e^{(\rho^{(2)}\Lambda_2 - \xi^{(2)})(t-\mathfrak{t})} d\mathfrak{t}.$$

B.3. Monitoring module $\mathcal{M}^{(3)}$

An upper bound on the magnitude of $\varepsilon_{zH}^{(3,1)}$ is computed as

$$|\varepsilon_{zH}^{(3,1)}| \le \Phi^{(3,1)}(t) \bar{\psi}^{(3,1)} + \int_0^t \left(\Phi^{(3,1)}(t-\mathfrak{t}) \Lambda_\gamma^{(3,1)} + \rho_d^{(3,1)} e^{-\xi_d^{(3,1)}(t-\mathfrak{t})} \bar{n}_z^{(3,1)} \right) d\mathfrak{t}, \tag{B.8}$$

where,

1. $|\varepsilon_{zH}^{(3,1)}(0)| = \bar{\psi}^{(3,1)} = \bar{z}^{(3,1)}$,
2. $|e^{-k_5 t}| \le \rho^{(3,1)} e^{-\xi^{(3,1)} t} = \Phi^{(3,1)}(t)$,
3. $|-k_5 e^{-k_5 t}| \le \rho_d^{(3,1)} e^{-\xi_d^{(3,1)} t}$,
4. $\Lambda_\gamma^{(3,1)} = \lambda_{\gamma_1^{(3)}} + |\frac{1}{a_2}| \lambda_{\gamma_3^{(3)}} + \frac{|a_1|}{|a_2|} \lambda_{\gamma_2^{(3)}} - \frac{|b_1||b_2|}{|a_2|} \bar{\tilde{\delta}}_p - \frac{|b_1|}{|a_2|} \bar{\tilde{\delta}}_p - \frac{|b_3||b_4|}{|a_2|} \bar{\tilde{\delta}}_s - \frac{|b_3|}{|a_2|} \bar{\tilde{\delta}}_s$,
5. $|n_z^{(3,1)}| \le \bar{n}_z^{(3,1)}$,

and $\lambda_{\gamma_1^{(3)}}$, $\lambda_{\gamma_2^{(3)}}$, and $\lambda_{\gamma_3^{(3)}}$ are the Lipschitz constants corresponding to ψ, r and $\dot{r}$, respectively; $(\bar{\tilde{\delta}}_p, \bar{\tilde{\delta}}_s)$ and $(\bar{\tilde{\delta}}_p, \bar{\tilde{\delta}}_s)$ are the upper limits on the respective thruster angles and their angular rates, respectively. The resulting adaptive threshold can be expressed by

$$\bar{\varepsilon}_{y_z}^{(3,1)}(t) = \rho^{(3,1)} e^{-\xi^{(3,1)} t} \bar{z}^{(3,1)} + \rho^{(3,1)} \Lambda_\gamma^{(3,1)} \int_0^t e^{-\xi^{(3,1)}(t-\mathfrak{t})} d\mathfrak{t} - \frac{\rho_d^{(3,1)} \bar{n}_z^{(3,1)}}{\xi_d^{(3,1)}} (1 - e^{-\xi_d^{(3,1)} t}) + \bar{n}_z^{(3,1)}. \tag{B.9}$$

B.4. Monitoring module $\mathcal{M}^{(4)}$

A bounded magnitude of the state estimation error under healthy conditions, $|\varepsilon_{zH}^{(4,1)}|$, can be described by

$$|\varepsilon_{zH}^{(4,1)}| \le \Phi^{(4,1)}(t) \bar{p}^{(4,1)} + \int_0^t \left(\Phi^{(4,1)}(t-\mathfrak{t}) \Lambda_\gamma^{(4,1)} - \rho_d^{(4,1)} e^{-\xi_d^{(4,1)}(t-\mathfrak{t})} \bar{n}_z^{(4,1)} \right) d\mathfrak{t}, \tag{B.10}$$

where,

1. $|\varepsilon_{zH}^{(4,1)}(0)| = \bar{p}^{(4,1)} = \bar{z}^{(4,1)}$,
2. $|e^{-K_6 t}| \le \rho^{(4,1)} e^{-\xi^{(4,1)} t} = \Phi^{(4,1)}(t)$,
3. $|-K_6 e^{-K_6 t}| \le \rho_d^{(4,1)} e^{-\xi_d^{(4,1)} t}$,

4. $\Lambda_{\gamma}^{(4,1)} = \begin{bmatrix} 2(\bar{u}+\bar{v}) + \bar{n}_u + \bar{n}_v \\ 2(\bar{u}+\bar{v}) + \bar{n}_u + \bar{n}_v \end{bmatrix}$, such that $z^{(4,2)} \leq \begin{bmatrix} \bar{u} & \bar{v} & \bar{r} \end{bmatrix}^T$ and $\bar{n}_z^{(4,2)} = \begin{bmatrix} \bar{n}_u & \bar{n}_v & \bar{n}_r \end{bmatrix}^T$,
5. $|n_z^{(4,1)}| \leq \bar{n}_z^{(4,1)}$.

Based on these computed bounds, the adaptive threshold can be expressed by

$$\bar{\varepsilon}_{y_z}^{(4,1)}(t) = \rho^{(4,1)} e^{-\xi^{(4,1)} t} \bar{z}^{(4,1)} + \rho^{(4,1)} \Lambda_{\gamma}^{(4,1)} \int_0^t e^{-\xi^{(4,1)}(t-\mathrm{t})} d\mathrm{t} - \frac{\rho_d^{(4,1)} \bar{n}_z^{(4,1)}}{\xi_d^{(4,1)}} (1 - e^{-\xi_d^{(4,1)} t}) + \bar{n}_z^{(4,1)}. \tag{B.11}$$

References

Abkowitz, M. A. (1980). Measurement of hydrodynamic characteristics from ship maneuvering trials by system identification. *SNAME Trans. 80*, 283–318.

Asfihani, T., Lutfiani, F., Widyotriatmo, A., & Hasan, A. (2024). Sensor fault diagnosis in autonomous ships. In *2024 European control conference (ECC)* (pp. 13–18). IEEE.

Benetazzo, F., Ippoliti, G., Longhi, S., & Raspa, P. (2015). Advanced control for fault-tolerant dynamic positioning of an offshore supply vessel. *Ocean Engineering*, *106*, 472–484.

Bhagavathi, R., Kufoalor, D. K. M., & Hasan, A. (2023). Digital twin-driven fault diagnosis for autonomous surface vehicles. *IEEE Access*, *11*, 41096–41104.

Blanke, M. (2006). Fault-tolerant sensor fusion for marine navigation. In *7th IFAC conference on maneuvering and control of marine craft* (pp. 1385–1390). Elsevier.

Closas, P., Fernandez-Prades, C., & Fernandez-Rubio, J. A. (2009). A Bayesian approach to multipath mitigation in GNSS receivers. *IEEE Journal of Selected Topics in Signal Processing*, *3*(4), 695–706.

Conejo, C., Puig, V., Morcego, B., Navas, F., & Milanés, V. (2025). Enhancing safety in autonomous vehicles using zonotopic LPV-EKF for fault detection and isolation in state estimation. *Control Engineering Practice*, *156*, 106192.

Cristofaro, A., & Johansen, T. A. (2014). Fault tolerant control allocation using unknown input observers. *Automatica*, *50*(7), 1891–1897.

Damen Shipyards Group (2025). Waterbus 2907 full electric. [Online; accessed: 2025-05-01]. https://www.damen.com/vessels/ferries/city-ferries/waterbus-2907-e3-full-electric.

Dhyani, A., Mojaveri, A. H., Zhang, C., Mahipala, D., Tran, H. A., Zhang, Y.-Y., Luo, Z., & Reppa, V. (2025). AUTOBargeSim: MATLAB (R) toolbox for the design and analysis of the guidance and control system for autonomous inland vessels. *To appear in the proceedings of the 16th IFAC conference on control applications in marine systems, robotics and vehicles*.

Dhyani, A., Negenborn, R. R., & Reppa, V. (2024a). A multiple sensor fault diagnosis scheme for autonomous surface vessels. *IFAC-PapersOnLine*, *58*(4), 31–36.

Dhyani, A., Wang, Y., Verbeke, M., Pissoort, D., & Reppa, V. (2024b). A POMDP model-based online risk mitigation method for autonomous inland vessels. *IFAC-PapersOnLine*, *58*(20), 335–340.

Du, Z., Negenborn, R. R., & Reppa, V. (2021). Cooperative multi-agent control for autonomous ship towing under environmental disturbances. *IEEE/CAA Journal of Automatica Sinica*, *8*(8), 1365–1379.

Fedyaevsky, K. K., & Sobolev, G. V. (1964). Control and stability in ship design.

Fossen, T. I. (2011). Handbook of marine craft hydrodynamics and motion control. John Wiley & Sons.

Fossen, T. I. (2022). Line-of-sight path-following control utilizing an extended kalman filter for estimation of speed and course over ground from GNSS positions. *Journal of Marine Science and Technology*, *27*(1), 806–813.

Fossen, T. I., & Strand, J. P. (1999). Passive nonlinear observer design for ships using lyapunov methods: Full-scale experiments with a supply vessel. *Automatica*, *35*(1), 3–16.

Gade, K. (2016). The seven ways to find heading. *The Journal of Navigation*, *69*(5), 955–970.

Groves, P. D. (2011). Shadow matching: A new GNSS positioning technique for urban canyons. *Journal of Navigation*, *64*(3), 417–430.

Kepaptsoglou, K., Fountas, G., & Karlaftis, M. G. (2015). Weather impact on containership routing in closed seas: A chance-constraint optimization approach. *Transportation Research Part C: Emerging Technologies*, *55*, 139–155.

Koh, K. K., & Yasukawa, H. (2012). Comparison study of a pusher–barge system in shallow water, medium shallow water and deep water conditions. *Ocean engineering*, *46*, 9–17.

Lin, Y., Du, J., Zhu, G., & Fang, H. (2018). Thruster fault-tolerant control for dynamic positioning of vessels. *Applied Ocean Research*, *80*, 118–124.

Liu, J., Hekkenberg, R., Rotteveel, E., & Hopman, H. (2015). Literature review on evaluation and prediction methods of inland vessel manoeuvrability. *Ocean Engineering*, *106*, 458–471.

Liu, Z., Zhang, Y., Yu, X., & Yuan, C. (2016). Unmanned surface vehicles: An overview of developments and challenges. *Annual Reviews in Control*, *41*, 71–93.

Marley, M., Skjetne, R., Gil, M., & Krata, P. (2023). Four degree-of-freedom hydrodynamic maneuvering model of a small azipod-actuated ship with application to onboard decision support systems. *IEEE Access*, *11*, 58596–58609.

Nomoto, K., Taguchi, T., Honda, K., & 9 Hirano, S. (1957). On the steering qualities of ships. *International Shipbuilding Progress*, *4*(35), 354–370.

Ogawa, A., Koyama, T., & Kijima, K. (1977). MMG report-I, on the mathematical model of ship manoeuvring. *Journal of the Society of Naval Architects of Japan*, *575*(22–28).

Park, B. S., & Yoo, S. J. (2016). Fault detection and accommodation of saturated actuators for underactuated surface vessels in the presence of nonlinear uncertainties. *Nonlinear Dynamics*, *85*(2), 1067–1077.

Reppa, V., Polycarpou, M. M., & Panayiotou, C. G. (2013). Adaptive approximation for multiple sensor fault detection and isolation of nonlinear uncertain systems. *IEEE Transactions on Neural Networks and Learning Systems*, *25*(1), 137–153.

Reppa, V., Polycarpou, M. M., Panayiotou, C. G. et al. (2016). Sensor fault diagnosis. *Foundations and Trends® in Systems and Control*, *3*(1–2), 1–248.

Rogne, R. H., Johansen, T. A., & Fossen, T. I. (2014). Observer and IMU-based detection and isolation of faults in position reference systems and gyrocompasses with dual redundancy in dynamic positioning. In *2014 IEEE Conference on control applications (CCA)* (pp. 83–88). IEEE.

Rogne, R. H., Johansen, T. A., & Fossen, T. I. (2015). On attitude observers and inertial navigation for reference system fault detection and isolation in dynamic positioning. In *2015 European control conference (ECC)* (pp. 3665–3672). IEEE.

Skjetne, R., Smogeli, Ø. N., & Fossen, T. I. (2004). A nonlinear ship manoeuvering model: Identification and adaptive control with experiments for a model ship. *Modeling, Identification and Control*, *25*(1), 3–27.

Song, J., & He, X. (2023). Robust state estimation and fault detection for autonomous underwater vehicles considering hydrodynamic effects. *Control Engineering Practice*, *135*, 105497.

Tahk, M., & Speyer, J. L. (1990). Target tracking problems subject to kinematic constraints. *IEEE Transactions on Automatic Control*, *35*(3), 324–326.

Tsolakis, A., Ferranti, L., & Reppa, V. (2024). Active thruster fault diagnosis for an overactuated autonomous surface vessel. *IFAC-PapersOnLine*, *58*(4), 43–48.

Vantorre, M., Eloot, K., Delefortrie, G., Lataire, E., Candries, M., & Verwilligen, J. (2017). Maneuvering in shallow and confined water. In *The encyclopedia of marine offshore engineering* (pp. 1–17).

Wang, N., Pan, X., & Su, S.-F. (2020). Finite-time fault-tolerant trajectory tracking control of an autonomous surface vehicle. *Journal of the Franklin Institute*, *357*(16), 11114–11135.

Wang, X., Wang, Q., Cao, X., Ouyang, Y., & Sun, C. (2024). State recovery and fault-tolerant control of autonomous surface vehicle with actuator and sensor faults. *IEEE Transactions on Intelligent Vehicles*, *10*(2), (pp. 1–12).

Yasukawa, H., & Yoshimura, Y. (2015). Introduction of MMG standard method for ship maneuvering predictions. *Journal of Marine Science and Technology*, *20*, 37–52.

Zhang, C., Cao, C., Guo, C., Li, T., & Guo, M. (2021a). Navigation multisensor fault diagnosis approach for an unmanned surface vessel adopted particle-filter method. *IEEE Sensors Journal*, *21*(23), 27093–27105.

Zhang, C., Dhyani, A., Ringsberg, J. W., Thies, F., Negenborn, R. R., & Reppa, V. (2025). Nonlinear model predictive control for path following of autonomous inland vessels in confined waterways. *Ocean Engineering*, *334*, 121592.

Zhang, C., Ma, Y., Thies, F., Ringsberg, J. W., & Xing, Y. (2024a). Towards autonomous inland shipping: A manoeuvring model in confined waterways. *Ships and Offshore Structures*, *20*(6), (pp. 1–13).

Zhang, C., Zhou, Z., Ning, P., Ming, Z., Zhang, C., & Fang, L. (2024b). IBRNet: Interpretable belief rule network modeling method for fault diagnosis of redundant inertial navigation systems. *Control Engineering Practice*, *144*, 105822.

Zhang, Q., Zhang, X., Zhu, B., & Reppa, V. (2021b). Fault tolerant control for autonomous surface vehicles via model reference reinforcement learning. In *2021 60th IEEE conference on decision and control (CDC)* (pp. 1536–1541). IEEE.

Zhou, Z., Zhong, M., & Wang, Y. (2019). Fault diagnosis observer and fault-tolerant control design for unmanned surface vehicles in network environments. *IEEE Access*, *7*, 173694–173702.

Zidan, J., Adegoke, E. I., Kampert, E., Birrell, S. A., Ford, C. R., & Higgins, M. D. (2021). Gnss vulnerabilities and existing solutions: A review of the literature. *IEEE Access*, *9*, 153960–153976.